



**HAL**  
open science

# A local damage model of concrete structures by a variational approach including tension and compression mechanisms

Céline Acary-Robert, Vincent Acary

► **To cite this version:**

Céline Acary-Robert, Vincent Acary. A local damage model of concrete structures by a variational approach including tension and compression mechanisms. 2020. hal-02864665

**HAL Id: hal-02864665**

**<https://hal.science/hal-02864665>**

Preprint submitted on 11 Jun 2020

**HAL** is a multi-disciplinary open access archive for the deposit and dissemination of scientific research documents, whether they are published or not. The documents may come from teaching and research institutions in France or abroad, or from public or private research centers.

L'archive ouverte pluridisciplinaire **HAL**, est destinée au dépôt et à la diffusion de documents scientifiques de niveau recherche, publiés ou non, émanant des établissements d'enseignement et de recherche français ou étrangers, des laboratoires publics ou privés.

# A local damage model of concrete structures by a variational approach including tension and compression mechanisms.

Céline Acary-Robert, Vincent Acary

11/06/2020

## Contents

|          |   |           |
|----------|---|-----------|
| <b>1</b> | <b>Introduction</b>   | <b>3</b>  |
| <b>2</b> | <b>A variational model for damage of concrete</b>                                       | <b>5</b>  |
| 2.1      | The elastic stiffness tensor evolution with damage . . . . .                            | 6         |
| 2.2      | Variational approach to damage . . . . .  | 7         |
| <b>3</b> | <b>Analysis of the damage model for Euler-Bernoulli beams</b>                           | <b>8</b>  |
| 3.1      | Basics on Euler-Bernoulli beam subjected a line load . . . . .                          | 8         |
| 3.2      | <i>A priori</i> analytical estimate of the damaged domain . . . . .                     | 9         |
| 3.3      | Numerical simulations with the damage model in 1D . . . . .                             | 14        |
| 3.3.1    | Sensitivity experiments . . . . .   | 16        |
| 3.3.2    | Realistic scenario of avalanches . . . . .  | 19        |
| 3.3.3    | Discussion . . . . .  | 20        |
| <b>4</b> | <b>A variational model with tension and compression damage mechanisms</b>               | <b>20</b> |
| 4.1      | Definition of the constitutive law . . . . .  | 21        |
| 4.2      | Damage evolution . . . . .  | 22        |
| 4.3      | Numerical implementation . . . . .  | 22        |
| <b>5</b> | <b>A case study on avalanche prevention structures</b>                                  | <b>24</b> |
| 5.1      | Validation and sensitivity experiments . . . . .  | 24        |
| 5.1.1    | Validation of the model: tension, compression, cyclic and bending experiments . . . . . | 25        |
| 5.1.2    | Three-point flexural test . . . . .   | 36        |
| 5.2      | Realistic configuration . . . . .   | 38        |



---

# Abstract

The present work aims at providing a numerical method to estimate the damage of a concrete structure, under the load of an avalanche-type natural event. Using the Francfort and Marigo damage model, we begin by validating the model in a 1-D configuration by analytical and numerical calculus. Moreover, as concrete has very different behaviour in tension and compression, we then introduce a tension-compression formulation in a 2-D configuration within the variational approach to damage. Considering a non-vanishing resulting Young modulus and minimizing the total energy, including the energy released by damage, provides us with the damage state during the load, without resorting to non-local formulation. We present some validation simulations such as three-point flexural test. Finally, we show realistic simulations of bending of the structure under the load of an avalanche and the resulting damaged state.

## 1 Introduction

In cold mountainous regions, under particular snow and weather conditions, avalanches are likely to produce important damages to people and buildings. Consequently, concrete structures are used to protect some areas and prevent these damages, supporting the load of the snow. The term of “avalanche” covers a range of various kinds of flows: dense, aerosol flows, multilayer ones, with a large range of speed and amplitude. Dense flows are characterized by the relative low speed at the front (40 m/s) and the pressure exerted on the obstacle is increasing with the concerned amount of snow. Contrary to that, fronts of powder snow avalanches move at higher speed (up to 100 m/s) and the profile of the pressure along an obstacle is highly varying in time, the impact pressure being followed by a great depression due to the vertical flow of the snow. More often, the flows are generally composed by one dense layer at the bottom, an intermediate one and an aerosol layer at the top of the flow.

Concrete structures, under the action of loadings due to avalanches, are damaged before reaching partial or total fracture. This damage state represents the rate of microcrackings inside the material. These kind of structures has been studied with various mechanical damage models for example in [Bertrand et al., 2010] to provide a damage index of the structure.

In this article, we are interested in the study of the mechanical response of the structure to an impact produced by an avalanche flow. As we use the framework of quasi-static mechanics with continuous damage under small perturbations, we then focus on dense avalanches with quite low speed front, and on the forecast of the onset of damage.

In order to model the evolution of the damage in the structure, we use the Francfort and Marigo mechanical damage model based on a variational approach with the fundamental assumption that the resulting elastic modulus does not vanish when the material is fully damaged. The variational approach is based on the minimization of the total energy which yields, on turns, a natural numerical approach. The main advantage of this model, under the fundamental assumption, is to provide a stable solution, without resorting to a non-local or a second-order gradient model, [Francfort and Marigo, 1993].

---

Moreover, modeling concrete structures implies also to take into account the difference in behaviors between tension and compression. As these characteristics are not present in the original model of Francfort and Marigo, we extend it in that direction. Models that take into account a different material behavior in tension and in compression have already been developed in the literature, but largely consider that the elastic tensor vanishes when the material is fully damaged. For example, in [Mazars and Pijaudier-Cabot, 1989], a damage model with a differentiation tension-compression with two terms depending on the sign of the strain tensor and two damage variables is introduced. Another formulation can be found in [Bernard et al., 2012] in the context of Thick Level-Set method, which consists in introducing a modulation between tension and compression damage through a user defined coefficient  $\beta$ . In the context of the variational approach to fracture, or equivalently phase-field models, [Miehe et al., 2010b, Miehe et al., 2010a] introduced an anisotropic formulation of the functional of global energy to model the different behavior in tension and compression. Other anisotropic models of damage can be found in [Bleyer and Alessi, 2018] where the mixity of fracture modes is taken into account. In all these works, the objective is to model fracture in materials with a phase-field approach. The elastic modulus goes to zero when the material is fully damaged and this lead to severe instability that are regularized with a non-local model of damage and/or viscosity regularization (see discussion in part 2).

In the present work, we prefer to use a model with a non-zero elastic modulus when the material is fully damaged. This is justified by the fact that a) the mathematical and numerical framework based on a variational approach keeps its stability and its simplicity, b) we are mainly interested by the onset of damage in the structure, and c) the assumption of a non-zero elastic modulus for reinforced concrete is reasonable. We then introduce the formulation tension-compression introduced by Comi in [Comi, 2001] and modify it to incorporate the previous hypothesis.

One question is raised: assuming that we know the main characteristics of an avalanche, are we able to a priori estimate the critical load that reveals the onset of damage of a concrete structure under the effect of the snow pressure? One objective of this work is to calculate an *a priori* estimate of the damage, assuming that we know the complete pressure profile or at least the maximum value reached.

The paper is organized in four main sections. In Section 2, the general framework of the damage model used in this study is introduced. Section 3 is dedicated to the study of the damage zone *a priori* estimation on a 1-D beam in plane strains. First, we introduce an analytical solution of the problem, assuming that we know the specific constant load, and then, we validate this estimation by numerical simulations. In Section 4, we present a 2-D model of damage, including tension and compression mechanisms, as introduced by Comi in [Comi, 2001], and extended in the framework of Francfort and Marigo. In Section 5, the model is validated on several academic and more realistic numerical experiments. Finally, we present some realistic experiments of dense avalanche flows on a concrete structure. Section 6 concludes the article.

---

## 2 A variational model for damage of concrete

We consider that the material constitutive law of the structure follows a quasi-brittle behavior. This material is damaged if the applied pressure force applied is sufficiently high. In the model, the damage modelling the damage is represented by a function  $\chi(\mathbf{x}, t)$  which varies between 0 and 1. An increase in this damage state induces a softening of the material. Finally, damage is an irreversible process: the damage zone of the structure can only increase. The inner variable modelling the damage follows a yield law, depending on the strains in the material.

Models which represent damage evolution in an elastic material are numerous and can be classified into two main families. The first one is the family of local damage models. In these models, the damage rate of the material is represented by an inner scalar variable and depends on the values of the strain tensor at each local point. The induced system of equations is mathematically ill-posed (loss of ellipticity) and leads to physically unacceptable results. Moreover, this formulation, when implemented in finite elements framework, in order to perform numerical simulations, presents severe drawbacks and leads to unrealistic numerical results: when the number of elements of the mesh increases, the volume of the damaged zone tends to zero while failure occurs without energy dissipation ([Mazars et al., 1991], [Peerlings et al., 1996]). To avoid these drawbacks, non-local models have been developed: the damage evolution is computed using an averaging method over a vicinity of the local point and needs the introduction of a characteristic length scale. As these averages imply numerous additional calculus, algorithms have been developed to separate pure elastic computations (local) and damage computations (non-local) as in [Pijaudier-Cabot and Bazant, 1987]. Another way to overcome these difficulties is to introduce some gradient quantities (gradient of internal variables or higher order gradient of the displacement). As described in [Lorentz and Benallal, 2005], these formulations need adapted and sophisticated numerical algorithms to be solved efficiently. As stated by [Peerlings et al., 1996], these two approaches, non-local and higher-order continua, present qualitative similarities. To give to these nonlocal model a thermodynamic consistency, the damage evolution has also been treated in [Frémond and Nedjar, 1996] by introducing an inner variable in the free energy balance, through internal forces. This formulation not only depends on the damage state, but also on its gradient.

As developed in [Luege et al., 2018], the simulation of non-local interactions are done through the gradient damage and need a specific splitting of variable to be solved numerically. As shown in [Tanné et al., 2018], to accurately determine the onset and the propagation of cracks, the model needs to take into account gradient of damage, an internal length and a critical stress level. Under that conditions, variational phase-field models address the following issues associated with brittle fracture: scale effects, nucleation, the existence of a critical stress, and path prediction. Finally, models with gradient damage formulation, including only partial damage have been studied from a mathematical point of view and Thomas and Mielke in [Thomas and Mielke, 2010] have proven existence and regularity results. Note that Mardare in [Mardare, 2011], in the non-linear elasticity framework, showed the existence on a nonlinear Korn inequality and the existence of a minimizer of an energetic formulation of the associated problem.

Nevertheless, as we do not focus on macro-cracks and their propagation, but only on global damage state, to

tackle the problem of modeling the spatial-temporal evolution of the damage of concrete structures, we choose to follow the variational approach developed in [Francfort and Marigo, 1993] in quasi-statics under the assumption of small perturbations and a non-vanishing elastic modulus. The use of this model will imply to keep a residual damage state (the whole structure cannot be damaged), but it is not too restrictive as our main idea is to evaluate the global damaged state and not to localize the macro-cracks and their propagation.

## 2.1 The elastic stiffness tensor evolution with damage

We consider an elastic body as an open bounded set  $\Omega$  in  $\mathbb{R}^d$ , with a  $C^1$  boundary  $\Gamma$ . A point  $M$  in  $\mathbb{R}^d$  is defined by its coordinates  $\mathbf{x} = (x_i)_{i=1\dots d}$  in the reference frame  $(\mathbf{i}, \mathbf{j}, \mathbf{k})$ . Let us denote by  $\mathbb{M}_s^d \in \mathbb{R}^{d \times d}$ , the set of symmetric matrices and  $\mathbb{T}_s^l$  the set of symmetric tensor of order  $l$ . Let  $\mathbf{u}(\mathbf{x})$  be the displacement vector at a point  $\mathbf{x} \in \mathbb{R}^d$  and  $\boldsymbol{\varepsilon} \in \mathbb{T}_s^d$  be the strain tensor under the assumptions of small perturbations defined by

$$\boldsymbol{\varepsilon}(\mathbf{u}) = \nabla_s^T \mathbf{u}^T = \frac{1}{2}(\nabla \mathbf{u} + \nabla^T \mathbf{u}).$$

Let us define  $\boldsymbol{\sigma}(\mathbf{x}) \in \mathbb{T}_s^d$  the stress tensor.

At a time  $t_i$ , we consider that the domain  $\Omega$  is decomposed into two sub-domains: a sub-domain of sound material  $\Omega_0$  and a subdomain of damaged material  $\Omega_1$ , such that  $\overline{\Omega} = \overline{\Omega_0 \cup \Omega_1}$  and  $\Omega_0 \cap \Omega_1 = \emptyset$ . These two sub-domains are characterized by a “damage factor” evolving from sound material to damaged material, in space and time. Since the damage phenomenon is irreversible, a point  $\mathbf{x}_1$  that belongs to  $\Omega_1$  (damaged part of the domain) at time  $t_*$  stays in  $\Omega_1$  at every time  $t \geq t_*$ .

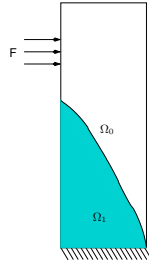


Figure 1: Sound and damaged domains, respectively  $\Omega_0$  and  $\Omega_1$  of the solid  $\Omega$ .

Hereafter, the damage evolution problem of the elastic material whose stiffness tensor drops from the sound value to the damaged one is presented following the pioneering work of [Francfort and Marigo, 1991]. The elastic stiffness tensor, denoted by  $\mathbf{E}(\mathbf{x}) \in \mathbb{T}_s^4$  depends on the local damage state at a point  $\mathbf{x}$ . Under the small strain assumption, the relation between the stress and strain tensors is assumed to be linear:

$$\boldsymbol{\sigma}(\mathbf{x}) = \mathbf{E}(\mathbf{x}) : \boldsymbol{\varepsilon}(\mathbf{u}(\mathbf{x})),$$

where the symbol “:” denotes the double contracted tensor product. In our model, the stiffness tensor is assumed to drop from  $\mathbf{E}_0$  in the sound domain  $\Omega_0$  to  $\mathbf{E}_1$  in the damaged domain  $\Omega_1$  with the following fundamental assumption:

$$\boldsymbol{\varepsilon} : \mathbf{E}_0 : \boldsymbol{\varepsilon} > \boldsymbol{\varepsilon} : \mathbf{E}_1 : \boldsymbol{\varepsilon} > 0, \quad \forall \boldsymbol{\varepsilon} \in \mathbb{T}_s^d, \quad (1)$$

that will be simply denoted in the sequel by  $\mathbf{E}_0 > \mathbf{E}_1 > 0$ .

We assume that damage is an irreversible process governed by a yield criterion and depending on the strain history ([Francfort and Marigo, 1991]).

If we denote by  $\chi$  the damage index at a position  $(\mathbf{x}, t)$  of the domain, the resulting stiffness tensor  $\mathbf{E}(\mathbf{x}, t)$  depends on time and  $\mathbf{x}$  position through the damage index  $\chi$  as:

$$\mathbf{E}(\chi(\mathbf{x}, t)) = (1 - \chi(\mathbf{x}, t))\mathbf{E}_0 + \chi(\mathbf{x}, t)\mathbf{E}_1 \quad (2)$$

Moreover, it is noteworthy that  $\chi$  is the characteristic function of the damaged domain.

The time interval of study  $[0, T]$  is decomposed into intervals  $]t_{i-1}, t_i]$  and a discrete incremental problem is solved on this time (loading) interval. The exponent  $i$  denotes the quantities at time  $t_i$ . Given the domain  $\Omega_1^{i-1}$  and its associated characteristic variable  $\chi^{i-1}(\mathbf{x})$  at time  $t_{i-1}$ , the incremental problem becomes:

$$\text{Find } \boldsymbol{\varepsilon}^i, \boldsymbol{\sigma}^i, \chi^i \text{ and } \mathbf{u}^i \text{ such that: } \quad 2\boldsymbol{\varepsilon}^i(\mathbf{u}(\mathbf{x})) = \nabla \mathbf{u}^i(\mathbf{x}) + \nabla \mathbf{u}^i(\mathbf{x})^T \quad \text{for all } \mathbf{x} \in \Omega \quad (3)$$

$$\boldsymbol{\sigma}^i(\mathbf{x}) = ((1 - \chi^i(\mathbf{x}))\mathbf{E}_0 + \chi^i(\mathbf{x})\mathbf{E}_1) : \boldsymbol{\varepsilon}^i(\mathbf{u}(\mathbf{x})) \quad \text{for all } \mathbf{x} \in \Omega \quad (4)$$

$$\text{div}(\boldsymbol{\sigma}^i(\mathbf{x})) + \mathbf{f}^i(\mathbf{x}) = 0 \quad \text{for all } \mathbf{x} \in \Omega \quad (5)$$

$$\Omega_1^{i-1} \subset \Omega_1^i \quad (6)$$

with the following boundary conditions:

$$\boldsymbol{\sigma}^i(\mathbf{x}) \cdot \mathbf{n}(\mathbf{x}) = \mathbf{T}^i(\mathbf{x}) \text{ on } \Gamma_1 \text{ and } \mathbf{u}^i(\mathbf{x}) = \mathbf{V}^i(\mathbf{x}) \text{ on } \Gamma_2 \quad (7)$$

where  $\mathbf{n}(\mathbf{x})$  is the normal vector on the boundary of the domain, the function  $\mathbf{f}^i(\mathbf{x})$  is the body forces,  $\mathbf{T}^i(\mathbf{x})$  the applied external force and  $\mathbf{V}^i(\mathbf{x})$  the prescribed displacement.

To complete the incremental problem, the constitutive law for the evolution of damage is developed in the sequel.

## 2.2 Variational approach to damage

In order to catch a stable solution of this problem, Francfort and Marigo proposed a variational approach that yields a stability criterion. The admissible solution must satisfy the incremental problem and also minimize the energy of the system. The classical mechanical problem at a time  $t_i$  is solved by finding a weak solution of the variational form of the system of equations (3)–(4)–(6) on the domain  $\Omega$ :

$$\int_{\Omega} \boldsymbol{\varepsilon}(\mathbf{u}^i(\mathbf{x})) : \mathbf{E}(\chi^i(\mathbf{x})) : \boldsymbol{\varepsilon}(\mathbf{v}^i(\mathbf{x})) dx = \int_{\Omega} \mathbf{f}^i(\mathbf{x}) \mathbf{v}^i(\mathbf{x}) dx + \int_{\Gamma} \mathbf{T}^i(\mathbf{x}) \mathbf{v}^i(\mathbf{x}) dx \quad (8)$$

Solving this weak formulation of the problem does not necessarily provides us with a stable solution.

Hence, Francfort and Marigo have chosen to solve the energetical formulation, introducing a stability criterion in the definition of the total energy of the system  $J$  at time  $t_i$ :

$$J(\mathbf{u}^i, \chi^i) = \frac{1}{2} \int_{\Omega} \boldsymbol{\varepsilon}(\mathbf{u}^i(\mathbf{x})) : \mathbf{E}(\chi^i(\mathbf{x})) : \boldsymbol{\varepsilon}(\mathbf{u}^i(\mathbf{x})) dx + \int_{\Omega} \kappa \chi^i(\mathbf{x}) dx - \int_{\Omega} f^i(\mathbf{x}) \mathbf{u}^i(\mathbf{x}) dx - \int_{\Gamma_1} T^i(\mathbf{x}) \mathbf{u}^i(\mathbf{x}) dx \quad (9)$$

with the remaining constraints

$$\begin{cases} \chi^{i-1} \leq \chi^i \leq 1 \\ \mathbf{u}^i(\mathbf{x}) = V^i(\mathbf{x}) \text{ on } \Gamma_2 \end{cases} \quad (10)$$

where  $\kappa$  is characteristic of the material and represents the dissipated energy by unit volume of the damage part of the domain.

They have shown in [Francfort and Marigo, 1993] that solving equations of system (3) under the constraints defined in (10) was equivalent to the following sequence of minimization problems:

$$\begin{aligned} \min_{\substack{(\chi^i, \mathbf{u}^i) \\ \chi^{i-1} \leq \chi^i \\ \mathbf{u}^i \in V_i}} J(\mathbf{u}^i(\mathbf{x}), \chi^i(\mathbf{x})) = & \min_{\substack{\chi^i \\ \chi^{i-1} \leq \chi^i}} \left( \min_{\mathbf{u}^i \in V_i} \frac{1}{2} \int_{\Omega} \boldsymbol{\varepsilon}(\mathbf{u}^i(\mathbf{x})) : \mathbf{E}^i(\chi^i(\mathbf{x}), \chi^i(\mathbf{x})) : \boldsymbol{\varepsilon}(\mathbf{u}^i(\mathbf{x})) dx \right. \\ & \left. + \int_{\Omega} \kappa \chi^i(\mathbf{x}) dx - \int_{\Omega} f^i(\mathbf{x}) \mathbf{u}^i(\mathbf{x}) dx - \int_{\Gamma_1} T^i(\mathbf{x}) \mathbf{u}^i(\mathbf{x}) dx \right) \end{aligned} \quad (11)$$

### 3 Analysis of the damage model for Euler-Bernoulli beams

In order to validate the model, we choose to apply it first in a simple 1-D configuration, given by a Euler-Bernoulli beam. The objective is to give some analytical insight on the damage evolution and to be able to analyze the different stages of the minimization.

#### 3.1 Basics on Euler-Bernoulli beam subjected a line load

Let  $L$  be the length of the beam and  $I$  the second moment of inertia of the cross area. We briefly recall that for a squared beam of thickness  $h$ , one gets  $I = \int_{-h/2}^{h/2} h z^2 dz = \frac{h^4}{12}$ . Let us consider a line load perpendicular to the axis of the beam given by  $p$ , such the beam supports a deformation due to bending (see Figure 2).

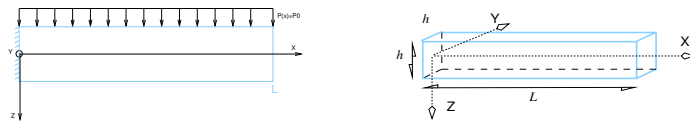


Figure 2: Clamped beam and axes

For this curvilinear model, the stiffness tensor is reduced to a scalar value  $E$  which depends on  $E_0$  value for the sound material and  $E_1$  for damaged material through the following relation:

$$E(\chi) = (1 - \chi)E_0 + \chi E_1. \quad (12)$$

In this configuration, solving (3) amounts to solving the equilibrium equation on a domain  $\Omega = (0, L)$  at each load increment  $i$ :

$$\frac{d^2}{dx^2} [E(\chi^i(x)) I \frac{d^2 u^i(x)}{dx^2}] = p^i(x). \quad (13)$$

where  $u(x) \in \mathbb{R}$  is the transverse displacement of the beam and  $x$  the abscissa, and  $E(\chi^i(x))$  the stiffness tensor defined in (12).

Noting  $\mathcal{V}$  the test functions set that satisfies the boundary conditions, we obtain the following expression for the weak formulation on the domain  $\Omega = [0, L]$ :

$$\int_{\Omega} \frac{d^2}{dx^2} [E(\chi^i(x)) I (u^i)'' ] v^i(x) dx = \int_{\Omega} p^i(x) v^i(x) dx \quad \forall v^i \in \mathcal{V}. \quad (14)$$

### 3.2 *A priori* analytical estimate of the damaged domain

The main objective of this part is to determine the critical pressure  $P_{min}$  to apply onto the beam to initiate the damage. We then have to solve the following equation, with  $\mathcal{U}$ , the set of admissible displacements.

$$\begin{aligned} \min_{(u_i, u_i'') \in \mathcal{U}} J(u_i, \chi_i(x)) &= \min_{(u_i, u_i'') \in \mathcal{U}} \frac{1}{2} \int_0^L I E_i(x) u_i''^2(x) dx + \int_0^L \kappa \chi_i(x) dx - \int_0^L p_i(x) u_i(x) dx \\ &= \min_{(u_i, u_i'') \in \mathcal{U}} \frac{1}{2} \int_0^L L(x, u_i, u_i'') dx \\ \text{such that} \quad u_i(0) &= 0; \quad u_i''(L) = 0 \\ \chi_{i-1}(x) &\leq \chi_i(x), \quad \forall x \in \Omega \end{aligned} \quad (15)$$

The *a priori* estimation of the damaged zone from the energy formulation and classical estimation tools such as Korn inequality does not lead to pertinent results due to the additional terms that cannot be easily estimated. We have quickly noted that the problem formulation was not suited for this kind of estimates because we have not been able to establish a relation between the damage zone quantity and the applied pressure load in a satisfying way. We then decided to tackle it in a direct way by searching for the minimum of the energy depending on the parameters of our problem. This calculus will be done in various steps: we first solve the Euler-Lagrange equation to get an expression of  $u_i''$ , we then define the associated energy function and finally get an expression of the critical load.

#### Solving Euler-Lagrange equation

First, we suppose that the constraint applied on the beam is a constant function:  $p_i(x) = P_{0,i}, \forall x \in [0, L]$ . By integrating two times the relation (13) between  $x$  and  $L$ , we get:

$$u_i''(x) = \frac{P_{0,i} (x - L)^2}{2I [(1 - \chi_i(x))E_0 + \chi_i(x)E_1]} \quad (16)$$

Two more integrations of equation (16) are needed to get an expression of  $u_i$ .

To go further in our analytic approach, we also assume that the damaged domain is continuous from the clamped point  $x = 0$  up to a point of the beam denoted by  $\alpha_i$ . The function  $\chi_i(x)$  is then defined on the interval  $[0, L]$  by:

$$\chi_i(x) = 1, \quad \forall x \in [0, \alpha_i) \text{ and } \chi_i(x) = 0, \quad \forall x \in [\alpha_i, L]. \quad (17)$$

The value  $\alpha_i$  is also the measure of the damage domain at time  $t_i$ :

$$\alpha_i = \int_0^L \chi_i(x) dx. \quad (18)$$

For each interval  $[0, \alpha_i)$  and  $[\alpha_i, L]$ , the calculus of the functions ( $u_i'$  and  $u_i''$ ) must distinguish two cases:

$$\begin{aligned} 0 \leq x < \alpha_i, \quad \chi_i(x) = 1, \quad u(x, \alpha_i) &= \frac{P_{0,i}}{2IE_1} \left[ \frac{(x-L)^4}{12} - \frac{L^4}{12} + \frac{L^3x}{3} \right] \\ \alpha_i \leq x \leq L, \quad \chi_i(x) = 0, \quad u(x, \alpha_i) &= \frac{P_{0,i}}{2IE_1} \left[ \frac{(\alpha_i - L)^4}{12} - \frac{L^4}{12} + \frac{L^3\alpha_i}{3} \right] \\ &+ \frac{P_{0,i}}{2IE_0} \left[ \frac{(x-L)^4}{12} - \frac{(\alpha_i - L)^4}{12} + \frac{L^3(x - \alpha_i)}{3} \right] \\ &- \frac{P_{0,i}}{2IE_1} \left[ \frac{(\alpha_i - L)^3}{3} + \frac{L^3}{3} \right] \frac{E_1 - E_0}{E_0} (x - \alpha_i) \end{aligned} \quad (19)$$

### Definition of the energy function

From equations (16) and (19), we obtain a new formulation for the energy function at time  $t_i$ :

$$\begin{aligned} J(u_i(x, \alpha_i), \chi_i(x)) &= \int_0^L \frac{1}{2} I E (\chi_i(x)) u_i''^2(x) dx + \int_0^L \kappa \chi_i(x) dx - \int_0^L P_{0,i} u_i(x, \alpha_i) dx \\ &= \int_0^L I [(1 - \chi_i(x)) E_0 + \chi_i(x) E_1] \left[ \frac{P_{0,i}^2}{8I^2} (x - L)^4 \left[ \frac{(1 - \chi_i(x))}{E_0} + \frac{\chi_i(x)}{E_1} \right]^2 \right] dx \\ &+ \int_0^L \kappa \chi_i(x) dx - \int_0^L P_{0,i} u_i(x, \alpha_i) dx \end{aligned} \quad (20)$$

Integrating the previous equation, we obtain:

$$J(\alpha_i) = \frac{-P_{0,i}^2(E_0 - E_1)}{40IE_0E_1} (\alpha_i - L)^5 + \kappa \alpha_i + \frac{P_{0,i}^2(7E_0 - 10E_1)}{120IE_0E_1} L^5 \quad (21)$$

Equation (21) depends only on  $\alpha_i$  and therefore can be differentiated with respect to  $\alpha_i$ . One gets:

$$J'(\alpha_i) = \kappa - \frac{P_{0,i}^2(E_0 - E_1)}{8IE_0E_1} (\alpha_i - L)^4 \quad (22)$$

Finally, the explicit calculus of  $J''$  shows that on the interval  $[0, L]$ ,  $J''$  is always strictly positive ensuring the convexity of  $J$ , and then the uniqueness of the minimizer.

### Calculus of the critical load to damage

In this section, an analytical expression of the damaged length  $\alpha_i$  with respect to the load  $P_{0,i}$  is given by solving

explicitly the minimization problem. Due to the assumption on the geometry of the damaged length, this calculus also provides us with the critical load  $P_c$  for which the damages length increases for a given  $\alpha_{i-1}$ , because in this special configuration test case, the damage at time  $t_i$  does not depend on historic of loads.

At time  $t_i$ , we apply a load  $P_{0,i}$  on the beam and the previous damaged domain  $\alpha_{i-1}$  is assumed to be known. To evaluate the current damaged domain  $\alpha_i$ , the following minimization problem must be solved:

$$\begin{aligned} \min \quad & J(\alpha_i) \\ \text{subject to} \quad & \alpha_{i-1} \leq \alpha_i \leq L \end{aligned} \quad (23)$$

To simplify the formulation of the optimality conditions, we introduce the vectors  $a^T = [1 \quad -1]$  and  $b^T = [\alpha_{i-1} \quad -L]$  such that the constraints are  $a \alpha_i - b \geq 0$ . Since the function  $J(\alpha_i)$  is convex and the feasible domain is also convex, the minimization problem (23) is equivalent to the Karush–Kuhn–Tucker conditions:

$$\begin{cases} J'(\alpha_i) - a^T \lambda = 0 \\ 0 \leq a \alpha_i - b \perp \lambda \geq 0, \end{cases} \quad (24)$$

where  $\lambda \in \mathbb{R}^2$  is a Lagrange multiplier. Substituting the  $a$  and  $b$ , we obtain

$$\begin{cases} J'(\alpha_i) - \lambda_1 + \lambda_2 = 0 \\ 0 \leq \lambda_1 \perp \alpha_i - \alpha_{i-1} \geq 0 \\ 0 \leq \lambda_2 \perp L - \alpha_i \geq 0. \end{cases} \quad (25)$$

Solving the complementarity system (25) provides us with an optimal point noted  $\alpha_i^*$ . Depending on the set of active constraints at optimality, three cases must be distinguished that corresponds to different behaviours of the beam:

1.  $\lambda_1 \geq 0, \lambda_2 = 0, \alpha_i^* = \alpha_{i-1}, 0 \leq J'(\alpha_i^*) = \lambda_1 \geq 0$  (no increase of the damage zone)

The applied load  $P_{0,i}$  is too small to increase the damaged domain that remains unchanged, *i.e.*,  $\alpha_i^* = \alpha_{i-1}^*$ . The gradient  $J'(\alpha_i^*)$  given in (21) must be positive which leads to the following upper bound for the load to keep a constant damaged zone:

$$P_{0,i} < \frac{2\sqrt{2\kappa E_0 E_1 I}}{(L - \alpha_{i-1})^2 \sqrt{(E_0 - E_1)}} = P_c(\alpha_{i-1}) \quad (26)$$

This last equation (26) provides us with a critical load  $P_c(\alpha_{i-1})$  under which the damage domain does not evolve from a given  $\alpha_{i-1}$ . This function is depicted in Figure 4a. If the beam was completely sound at the previous loading step ( $\alpha_{i-1} = 0$ ), we obtain the critical pressure for  $P_{0,i}$  to start to damage of the beam:

$$P_{\min} = P_c(0) = \frac{2\sqrt{2\kappa E_0 E_1 I}}{L^2 \sqrt{(E_0 - E_1)}} \quad (27)$$

2.  $\lambda_1 = \lambda_2 = 0$ ,  $\alpha_{i-1} < \alpha_i^* < L$ ,  $J'(\alpha_i^*) = 0$  (increase of the damage zone)

The condition  $J'(\alpha_i^*) = 0$  leads to the value of the damaged zone with respect to the applied load:

$$\alpha_i^* = L - \left( \frac{8\kappa E_0 E_1 I}{(E_0 - E_1) P_{0,i}^2} \right)^{1/4} \quad (28)$$

The inequality  $\alpha_{i-1} < \alpha_i^*$  yields a condition on the applied load that must be sufficiently high to increase the damage of the beam. Due to the complementarity in the optimality condition, we obtain

$$P_{0,i} \geq P_c(\alpha_{i-1}). \quad (29)$$

Note that the value of the damaged zone with respect to the applied load in (28) does not depend on  $\alpha_{i-1}$ . The relation (28) may be understood as the level of damage of the beam for a given continuously increasing load  $P_{0,i}$ . This relation appears as the inverse of the relation (26) and is illustrated in Figure 4b.

3.  $\lambda_2 \geq 0$ ,  $\lambda_1 = 0$ ,  $\alpha_i^* = L$ ,  $J'(\alpha_i^*) = -\lambda_2 \leq 0$  (full damage of the beam)

In the last case, the applied load  $P_{0,i}$  must be sufficiently large to damage all the domain. For  $\alpha_i = L$ , we obtain for the gradient

$$J'(\alpha_i) = \kappa > 0 \quad (30)$$

which contradicts the optimality conditions. This case is not a valid solution. This conclusion is consistent with the previous relations (26) and (28), from which we can remark that

$$\lim_{\alpha_{i-1} \rightarrow L} P(\alpha_{i-1}) = +\infty, \quad \text{and } \alpha_i^* < L \text{ for any } P_{0,i} < +\infty. \quad (31)$$

| Numerical parameters                   |                                   |
|--|-----------------------------------|
| Total length of the beam               | $L = 2$ m                         |
| Thickness of the beam                  | $h = 0.1$ m, $I = \frac{h^4}{12}$ |
| Young coefficient for sound concrete   | $E_0 = 1.10^7$ Pa                 |
| Young coefficient for damaged concrete | $E_1 = 1.10^6$ Pa                 |
| Treshold value for damage              | $\kappa = 100$ J/m <sup>3</sup>   |
| Resulting critical pressure            | $P_{\min} = 68.04$ Pa             |

Table 1: Characteristic parameters of a 1-D beam for numerical illustrations

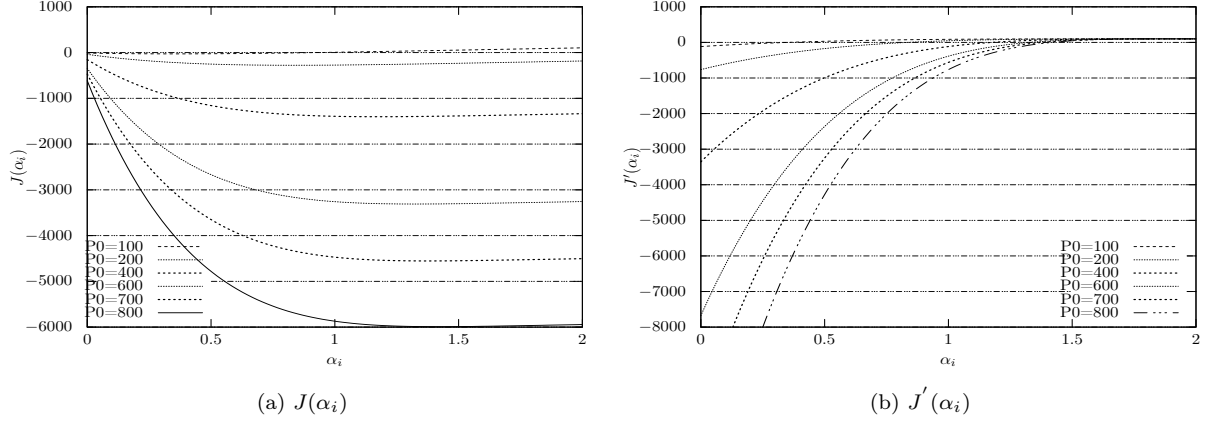
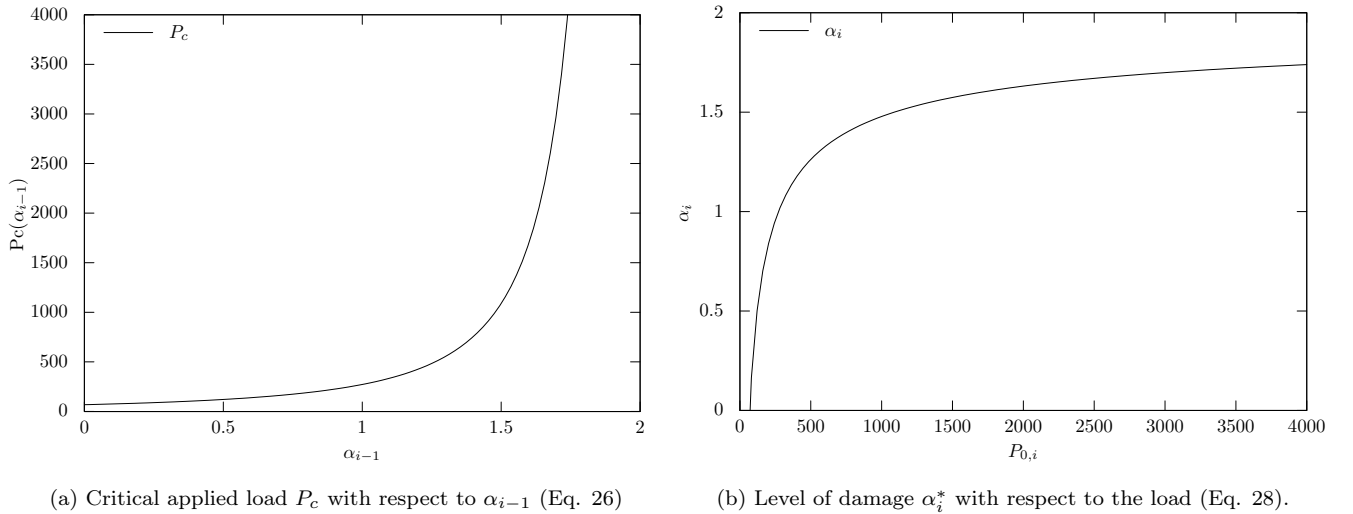


Figure 3:  $J$  and its derivative  $J'$  functions of  $P_{0,i}$ , from equations (21) and (22)

### Numerical illustrations

For different given values of  $P_{0,i}$ , the function  $J(\alpha_i)$  and its derivative are plotted in Figure 3a and 3b. One observes that the function  $J$  is convex and the maximum value of  $J'(\alpha_i)$  increases with  $P_{0,i}$ . In other words, when  $P_{0,i}$  increases the minimal value of  $J(\alpha_i)$  is shifted to the right.

Plotting the evolution of the critical load  $P_c$  with respect to the previous damage state of the beam in Figure 4a shows that to damage the beam more than roughly 80%, the load must increase very drastically, leading to infinite load to completely damage the beam.



(a) Critical applied load  $P_c$  with respect to  $\alpha_{i-1}$  (Eq. 26)

(b) Level of damage  $\alpha_i^*$  with respect to the load (Eq. 28).

Figure 4: Evolution of the critical load, function of the previous state  $\alpha_{i-1}$  (left) and evolution of the damage state, function of the load  $P_{0,i}$  (right).

### 3.3 Numerical simulations with the damage model in 1D

To validate the analytical solution obtained for a line load on a cantilever beam, the same problem is now solved using a FEM numerical approach. We perform the minimization with alternate directions using two steps for the function  $J$  built from energy estimation. The Euler-lagrange differential equation can be numerically solved using a classic weak formulation using finite elements discretization to find the displacement  $u_i$ , assuming a given value  $\chi_{i-1}$ . Then, the current damage state  $\chi_i$  is updated keeping the computed values of the displacement  $u_i$ .

#### Computation of the discrete displacements.

The discrete weak formulation equation:

$$\int_{\Omega_e} E^i(x) I \left[ \frac{d^2 u^i(x)}{dx^2} \right] \left[ \frac{d^2 v(x)}{dx^2} \right] dx = \int_{\Omega_e} p^i(x) v(x) dx \quad (32)$$

for all test functions  $v$  satisfying the boundary conditions.

The elementary displacement vector is defined as:  $u_e^i = \begin{bmatrix} u_1^i & \theta_1^i & u_2^i & \theta_2^i \end{bmatrix}$  with two degrees of freedom defined at each node of an element (a displacement and a rotation). The chosen finite elements shape functions matrix  $\mathbf{N}_e(x)$  is composed of cubic Hermite polynomials which allow  $C^1$  continuity between elements. The interpolation formulas are then given on each element  $e$  by:

$$u_e^i(x) = \begin{bmatrix} N_{e,v_1}(x) & N_{e,\theta_1}(x) & N_{e,v_2}(x) & N_{e,\theta_2}(x) \end{bmatrix} \begin{bmatrix} u_{e_1}^i \\ \theta_{e_1}^i \\ u_{e_2}^i \\ \theta_{e_2}^i \end{bmatrix} = \mathbf{N}_e(x) \mathbf{u}_e^i$$

and  $v_e(x) = \mathbf{N}_e(x) \mathbf{v}_e$ . By substitution in (32), the weak approximation is obtained for an element  $e$ :

$$\mathbf{v}_e^T \int_{\Omega_e} E^i(x) I \mathbf{N}_e''^T(x) \mathbf{N}_e''(x) dx \mathbf{u}_e^i = \mathbf{v}_e^T \int_{\Omega_e} \mathbf{N}_e^T(x) p_e^i(x) dx, \text{ for all } \mathbf{v}_e \quad (33)$$

which leads to the discrete equilibrium equation:

$$\mathbf{K}_e^i \mathbf{u}_e^i = \mathbf{F}_e^i, \quad (34)$$

with the stiffness matrix and the applied load vector defined by

$$\mathbf{K}_e^i = \int_{\Omega_e} E^i(x) I \mathbf{N}_e''^T(x) \mathbf{N}_e''(x) dx, \quad \mathbf{F}_e^i = \int_{\Omega_e} \mathbf{N}_e^T(x) p_e^i(x) dx. \quad (35)$$

One can note that the computation of the stiffness matrix  $\mathbf{K}_e^i$  on the element  $e$  depends on the function  $E^i(x) = E(\chi^i(x))$  which depends on the damage function  $\chi^i(x)$ . The choice of  $P2$  elements would have allowed a continuous description of the damage state on each element but in this first approximation of the problem, we have chosen to keep it constant element by element, providing that each one is little enough. This function  $E^i(x)$  is then piecewise constant on the beam. The assembled system  $\mathbf{K}^i \mathbf{u}^i = \mathbf{F}^i$  is obtained on each element as  $\mathbf{K}_e^i \mathbf{u}_e^i = \mathbf{F}_e^i$  under the assumption

that  $\chi^i(x) = \chi_e^i \in \{0, 1\}$ ,  $\forall x \in \Omega_e$ . The fact that  $E^i(x)$  is constant on each element  $e$  and its formulation is given by  $E^i(x) = (1 - \chi_e^i)E_0 + \chi_e^i E_1 = E_e^i, \forall x \in \Omega_e$ , leads to the following expression of  $\mathbf{K}_e^i$ :

$$\mathbf{K}_e^i = I \int_{\Omega_e} E_e^i \mathbf{N}_e''^T(x) \mathbf{N}_e''(x) dx = I E_e^i \int_{\Omega_e} \mathbf{N}_e''^T(x) \mathbf{N}_e''(x) dx \quad (36)$$

The external force matrix depends on the load on the direction  $x$  and as the load is supposed to be constant in space ( $p^i(x) = P_0^i, \forall x \in [0, L]$ ):

$$\mathbf{F}_e^i = \int_{\Omega_e} \mathbf{N}_e^T(x) p^i(x) dx = P_0^i \int_{\Omega_e} \mathbf{N}_e^T(x) dx \quad (37)$$

For a given damage state  $\chi^i$  piecewise constant over the elements, the displacements  $\mathbf{u}^i$  are computed by solving the linear system  $\mathbf{K}^i \mathbf{u}^i = \mathbf{F}^i$ .

### Calculus of the damaged state

Assuming that the function  $\chi(x)$  is approximated as a piecewise constant function on an element, the energy function  $J$  is given for each element  $e$  by:

$$\begin{aligned} J_e(\mathbf{u}_e^i, \chi_e^i) &= \frac{1}{2} I E_e^i \mathbf{u}_e^{iT} \left( \int_{\Omega_e} \mathbf{N}_e''^T(x) \mathbf{N}_e''(x) dx \right) \mathbf{u}_e^i + l_e \kappa \chi_e^i - P_0^i \mathbf{u}_e^{iT} \mathbf{F}_e^i \\ &= \frac{1}{2} \mathbf{u}_e^{iT} \mathbf{K}_e^i \mathbf{u}_e^i + l_e \kappa \chi_e^i - \mathbf{u}_e^{iT} \mathbf{F}_e^i \end{aligned}$$

where  $l_e$  is the length of the element  $e$ .

The total sum provides the expression of  $J$  for the whole beam:

$$J(\mathbf{u}^i, \chi^i) = \sum_{e=1}^N J_e(\mathbf{u}_e^i, \chi_e^i) = \sum_{e=1}^N \frac{1}{2} \mathbf{u}_e^{iT} \mathbf{K}_e^i \mathbf{u}_e^i + l_e \kappa \chi_e^i - \mathbf{u}_e^{iT} \mathbf{F}_e^i \quad (38)$$

At each iteration in time  $i$ , in order to know the damage state of the beam given on each element by  $\chi_e^i$ , we need to find the function  $\chi^i$ , at iteration  $i$ , which minimize the following discrete equation:

$$\min_{\chi} J(\mathbf{u}^i, \chi) \quad (39)$$

under the following constraints:

- $\chi_e \geq \chi_e^{i-1}$  for all  $e \in 0, \dots, N$ :  $\chi_e^i$  depends on the previous values of the damaged zone (damage is an irreversible process)
- $\chi_e \in \{0, 1\}$ , for all  $e \in 0, \dots, N$ :  $\chi_e^i$  function has discrete values in 0, 1.

In a first attempt, we have tried to use a fixed point method with a convergence criterium as Jouve *et al.* in [Allaire et al., 1998] but the convergence was difficult in our configuration. This problem can also be considered as a Mixed-Integer Programming Problem and solved with corresponding external library like for example `lp_solve`. But, finally, due to the hypothesis of our problem and to be able to verify each step, we have written an enumerative technique to find the minimum of the functional of energy. We test every case, under the hypothesis that the damage domain is propagating from the basis to the top and cannot present some discontinuities.

### 3.3.1 Sensitivity experiments

This part is dedicated to the study of the sensitivity of the numerical model to the parameters of the simulation, with various loading schemes. In a first part, we have tested the sensitivity of the model to the mesh size to find the critical load  $P_{\min}$  of the applied pressure for damaging the beam and then we analyzed the associated dissipated energy. Finally, we performed a sensitivity experiment to test the role of the size of the load step increment in pressure.

In a second part, we present some realistic avalanche test cases and their impact on the concrete structure. To build these scenarii, we have used the characteristic avalanche pressure impacts on a structure described in [Ancy et al., 2006], [Berthet-Rambaud et al., 2008] and [Bertrand et al., 2010] and our previous numerical results about the impact of avalanches on a beam ([Dutykh et al., 2011]). We retain mainly two avalanche schemes: a mono-layer avalanche flow and a three-layers flow. As the matter of fact, if we consider an approximation of an avalanche flow in a single-layer fluid flow, the pressure repartition along the concrete structure is supposed to be lightly higher at the bottom of the structure and its time evolution is composed of three main parts: a huge impact with a rapid pressure increase, then a stay at a threshold value and then followed by a less steep decrease (this evolution is detailed for example in [Berthet-Rambaud et al., 2008] and [Bertrand et al., 2010]). The majority of huge avalanches are multi-layers flows with a dense part at the bottom (characterized by a high pressure and a low velocity), a powder part at the top (lower pressure and higher velocities) and an intermediate part. To mimic this kind of avalanche, we can built a three layers scenario, with a time evolution of the pressure in intensity along the beam (not shown in this study).

|   |                                   |
|---|-----------------------------------|
| Numerical parameters                      |                                   |
| Total length of the beam                  | $L = 2$ m                         |
| Thickness of the beam                     | $h = 0.1$ m, $I = \frac{h^4}{12}$ |
| Young coefficient for sound concrete      | $E_0 = 2.10^{10}$ Pa              |
| Young coefficient for damaged concrete    | $E_1 = 3.10^9$ Pa                 |
| Damage parameter                          | $\kappa = 400$ J/m <sup>3</sup>   |
| Number of elements for the discretization | N=200                             |
| Analytical critical pressure              | $P_{\min} = 5976$ Pa              |

**Critical load for damage** We have seen that we were able to explicitly calculate the critical bound for the pressure  $P_{\min}$  assuming a specific geometry of the damaged zone. The first experiment is performed with an increasing load, uniformly distributed along the height. This first experiment helps us to determine if the numerical simulations allow to retrieve the same value, and the precision of the mesh we need to correctly catch the critical pressure.

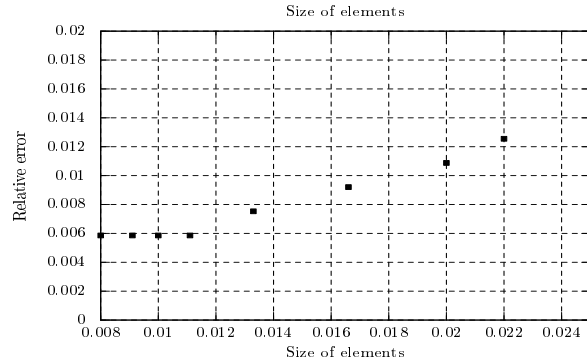


Figure 5: Relative error for the critical pressure  $P_{\min}$  with respect to the mesh size.

The theoretical critical load is  $P_{\min} = 5976$  Pa (found in the analytical study) and the relative error with respect to mesh size is represented in Figure 5. In this experiment, the pressure increment is  $\Delta P = 10$  Pa. We can remark that from 200 elements, for  $L = 2$  m that is to say  $\Delta x = 0.01$  m, the critical pressure is computed by the numerical approximation with a relative error less than  $6.10^{-3}$ .

**Dissipated energy by the damage of the beam** As detailed in Section 2, the main drawback of local damage models is characterized by an important dependence of the solution to the mesh size. Without homogenization, dissipated energy by damage depends on the mesh and tends to decrease with the size of elements. Contrary to that, the model proposed by Francfort and Marigo in [Francfort and Marigo, 1993] introduces a global minimisation of the energy in the whole structure and avoids this drawback for a value of  $E_1 > 0$ . The energy dissipation is represented in Figure 6. We can observe that the evolution of the dissipated energy by damage depends on the discretisation, but converges towards a finite limit curve.

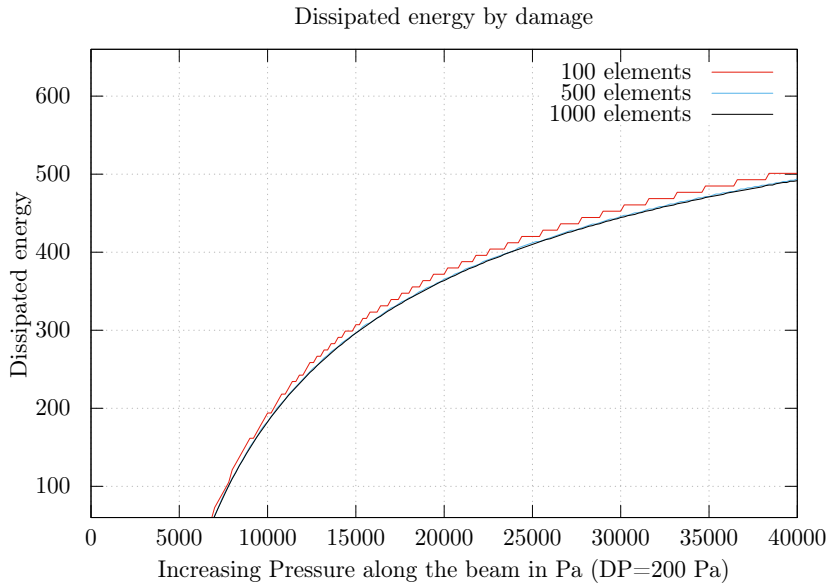


Figure 6: Dissipated energy by damage

**Sensitivity of the damaged part of the beam with respect to the number of elements** In this part, we present the sensitivity of the damage zone to the mesh size for  $P=40000$  Pa in Figure 7. The percentage of the damaged zone in the beam converges to a given value. Above 200 elements, the damaged part of the beam remains nearly unchanged.

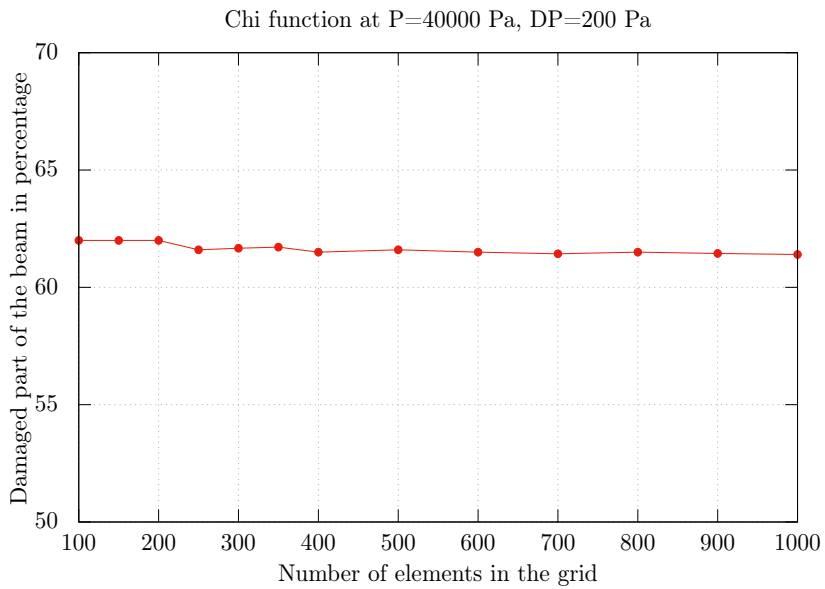


Figure 7: Damage part of the beam at  $P=40000$  Pa for different sizes of the grid

**Sensitivity of the damaged part of the beam with respect to the load step** The sensitivity of the damaged zone to the load step size is depicted in Figure 8, which illustrates the damaged part of the beam in percentage at the end of the experiment for different values of  $\Delta P = P_{0,i} - P_{0,i-1}$  up to the final load equal to 40000 Pa. For the given loading increments, the influence of the load size is very low.

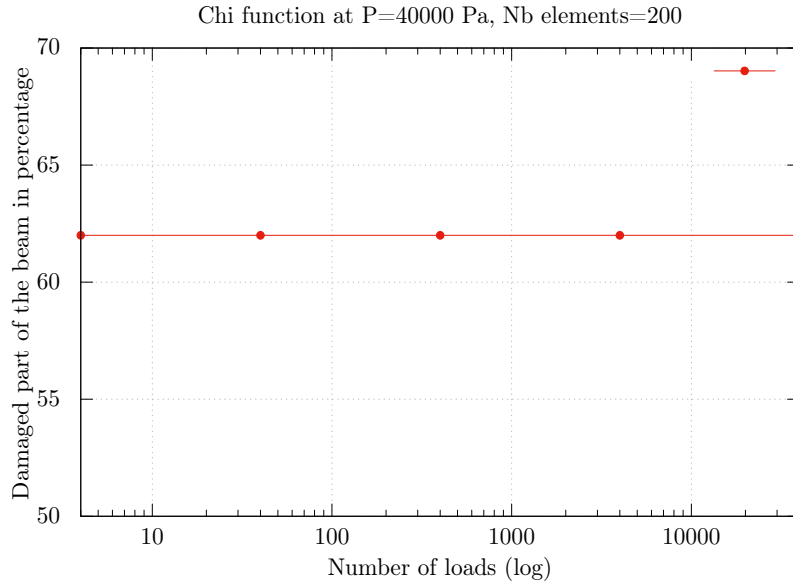


Figure 8: Damage part of the beam at P=40000 Pa for varying  $\Delta P$

### 3.3.2 Realistic scenario of avalanches

In this second part, we study a realistic scenario of loading. This is a class of realistic mono-layer avalanche with a constant load along the height of the beam. For this experiment, we have chosen a mesh size of  $\Delta x = 0.01$  m, which is sufficient to accurately capture the critical load (see Figure 5).

**Increasing loading in time and discharge** In this part, we highlight the irreversibility of the processus of damage. This scenario is built with an increasing part, a stable stage at a constant level of pressure followed by a discharge. In Figure 9b, we illustrate with bars the percentage of the damaged beam relative to the total height. We can see that above the critical load, the damaged part of the beam increases while the pressure load increases. And, as expected, we can see that the damaged part of the beam never decreases although the applied pressure decreases, showing the irreversibility of the damage mechanism. The top displacement of the beam is also correlated with the value of the load as we can see in Figure 9c.

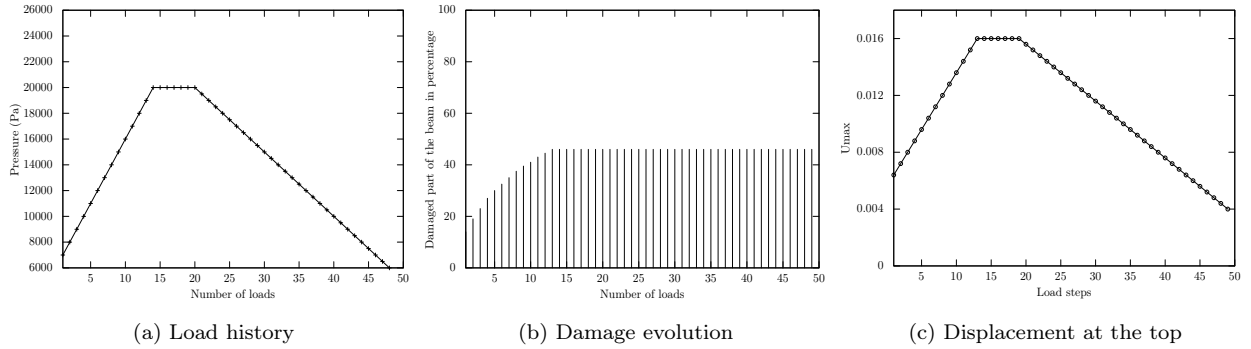


Figure 9: Load history, percentage of damaged beam and maximum bending

### 3.3.3 Discussion

The results in these 1D experiments show for one hand that the analytical results are validated by the numerical model. Above a given grid size, the critical load is well caught by the numerical model. As the matter of fact, we have seen that for mesh with elements under 0.012 m, the critical load remains nearly unchanged and the sensitivity to the mesh size is negligible. Moreover, the model is able to reproduce the irreversibility of the process and allows to underline the effects of the softening of the material and the difference induced in the tip displacement.

## 4 A variational model with tension and compression damage mechanisms

The damage model presented in Section 2 does not make any difference between the behaviour of the material in tension and compression, which is a severe drawback for quasi-brittle materials such as concrete or rock materials. In this section, we extend the model including a different evolution of the damage variable in tension and also in compression. To this aim, we formulate a new model with a non-zero elastic tensor when the material is fully damaged. The considered theoretical framework is still a variational approach to damage to keep the stability properties. Following the work in [Comi, 2001] and [Comi and Perego, 2001], we formulate the energy separated in two terms: a term using the positive part (reps. negative part) of the trace of the strains and an elastic modulus depending of the damage variable in tension (resp. in compression).

As explained in the introduction, in the present work, we use a model with a positive residual elastic modulus when the material is fully damaged to avoid instabilities.

## 4.1 Definition of the constitutive law

In [Comi, 2001], the constitutive law reads as:

$$\boldsymbol{\sigma}(\mathbf{u}) = \frac{E_0}{1+\nu}(1-\chi_t)(1-\chi_c)\boldsymbol{\varepsilon}^d(\mathbf{u}) + \frac{1}{3}\frac{E_0}{(1-2\nu)}(1-\chi_t)\text{tr}^+(\boldsymbol{\varepsilon}(\mathbf{u}))\mathbf{I} + \frac{1}{3}\frac{E_0}{(1-2\nu)}(1-\chi_c)\text{tr}^-(\boldsymbol{\varepsilon}(\mathbf{u}))\mathbf{I} \quad (40)$$

where  $\boldsymbol{\varepsilon}^d$  is the deviator part of the strain,  $E_0$  represents the Young modulus of the sound material and  $\chi_t$  and  $\chi_c$  are the damage variables respectively in tension and compression. The operator  $\text{tr}$  is the trace operator and the superscript  $+$  and  $-$  stand for the positive and the negative parts<sup>1</sup>. In this formulation, the equivalent elastic tensor vanishes if  $\chi_t = 1$  in traction, or  $\chi_c = 1$  in compression. We want to avoid this feature as in one hand we consider reinforced concrete with a residual elastic behavior, and on the other hand, from a mathematical point of view, it is a mandatory ingredient for the stability of the solution.

We propose here a new formulation for this equivalent elastic tensor that respects the drop of the elastic modulus from  $E_0$  (sound state) to  $E_1$  (damaged state), while distinguishing tension and compression by considering the following modified elastic moduli that depend on  $\chi_c$  and  $\chi_t$ :

$$\begin{aligned} E_d(\chi_t, \chi_c) &= E_0(1 + \chi_t\chi_c - \chi_t - \chi_c) + E_1(\chi_t + \chi_c - \chi_t\chi_c) \\ E_t(\chi_t) &= E_0(1 - \chi_t) + E_1(\chi_t) \\ E_c(\chi_c) &= E_0(1 - \chi_c) + E_1(\chi_c) \end{aligned} \quad (41)$$

with the modified constitutive law as follows:

$$\boldsymbol{\sigma}(\mathbf{u}) = \frac{E_d(\chi_t, \chi_c)}{1+\nu}\boldsymbol{\varepsilon}^d(\mathbf{u}) + \frac{1}{3}\frac{E_t(\chi_t)}{(1-2\nu)}\text{tr}^+(\boldsymbol{\varepsilon}(\mathbf{u}))\mathbf{I} + \frac{1}{3}\frac{E_c(\chi_c)}{(1-2\nu)}\text{tr}^-(\boldsymbol{\varepsilon}(\mathbf{u}))\mathbf{I} \quad (42)$$

With this model, considering a complete damage state in tension or in compression, that is to say  $\chi_t = 1$  or  $\chi_c = 1$  leads to a value of  $E_1$  for the Young modulus. More precisely, it is easy to check that

$$\begin{aligned} E_d(1, \chi_c) &= E_1 \text{ and } E_d(\chi_t, 1) = E_1 \\ E_t(1) &= E_1 \\ E_c(1) &= E_1 \end{aligned} \quad (43)$$

To simplify the notation, we introduce the elastic tensors  $\mathbf{E}_d$ ,  $\mathbf{E}_t$  and  $\mathbf{E}_c$  in  $\mathbb{T}_s^4$  that can be easily identified from (42) to obtain:

$$\boldsymbol{\sigma}(\mathbf{u}) = \mathbf{E}_d(\chi_t, \chi_c) : \boldsymbol{\varepsilon}^d(\mathbf{u}) + \frac{1}{3}\mathbf{E}_t(\chi_t) : \text{tr}^+(\boldsymbol{\varepsilon}(\mathbf{u})) : \mathbf{I} + \frac{1}{3}\mathbf{E}_c(\chi_c) : \text{tr}^-(\boldsymbol{\varepsilon}(\mathbf{u})) : \mathbf{I}. \quad (44)$$

The free energy associated to the model in (44) is given by

$$\psi(\mathbf{u}, \chi_t, \chi_c) = \frac{1}{2} \left( \boldsymbol{\varepsilon}^d(\mathbf{u}) : \mathbf{E}_d(\chi_t, \chi_c) : \boldsymbol{\varepsilon}^d(\mathbf{u}) + \frac{1}{3}\boldsymbol{\varepsilon}(\mathbf{u}) : \mathbf{E}_t(\chi_t) : \text{tr}^+(\boldsymbol{\varepsilon}(\mathbf{u}))\mathbf{I} + \frac{1}{3}\boldsymbol{\varepsilon}(\mathbf{u}) : \mathbf{E}_c(\chi_c) : \text{tr}^-(\boldsymbol{\varepsilon}(\mathbf{u}))\mathbf{I} \right). \quad (45)$$

<sup>1</sup>For a scalar  $x = x^+ + x^-$ , with  $x^+ = x$  if  $x \geq 0$  and 0 if  $x < 0$  and,  $x^- = x$  if  $x \leq 0$  and 0 if  $x > 0$ .

## 4.2 Damage evolution

As in the isotropic case in Section 2, the damage state  $\chi^i$  and the displacement  $\mathbf{u}^i$  at each time  $t_i$  and each load  $\mathbf{f}^i$  are given by minimizing the following functional of energy over the displacement  $\mathbf{u}$  and the damage state  $(\chi_c, \chi_t)$ :

$$J(\mathbf{u}(\mathbf{x}), \chi_t(\mathbf{x}), \chi_c(\mathbf{x})) = \int_{\Omega} \psi(\mathbf{u}(\mathbf{x}), \chi_t(x), \chi_c(x)) dx + \int_{\Omega} \kappa_t \chi_t(\mathbf{x}) dx + \int_{\Omega} \kappa_c \chi_c(\mathbf{x}) dx - \int_{\Omega} \mathbf{f}^i(\mathbf{x}) \mathbf{u}(\mathbf{x}) dx - \int_{\Gamma} T^i(\mathbf{x}) \mathbf{u}^i(\mathbf{x}) dx \quad (46)$$

subjected to the constraints:

$$\begin{cases} \chi_t^{i-1} \leq \chi_t^i \leq 1 \\ \chi_c^{i-1} \leq \chi_c^i \leq 1 \\ \mathbf{u}^i \in V_i. \end{cases} \quad (47)$$

The constant  $\kappa_c$  and  $\kappa_t$  are respectively the damage parameters for compression and traction.

## 4.3 Numerical implementation

To solve our problem, we use an algorithm based on alternating directions: first, we calculate the displacement field at time  $t_i$  by solving a non-linear problem for a given  $\chi_{i-1}$ , and then we minimize the energy function to find the corresponding damage state  $\chi_i$ , with a Quasi-Newton method. The nonlinear problem for computing displacement is nonsmooth and is solved with a semi-smooth Newton method; the algorithm is initialized with the solution of the equivalent linearized system.

### Calculus of the displacement

The free energy can be decomposed in the total strain and a trace term:

$$\psi(\mathbf{u}, \chi_t, \chi_c) = \frac{1}{2} \left( \boldsymbol{\varepsilon}(\mathbf{u}) : \mathbf{E}_d : \boldsymbol{\varepsilon}(\mathbf{u}) - \frac{1}{3} \boldsymbol{\varepsilon}(\mathbf{u}) \mathbf{E}_d \operatorname{tr}(\boldsymbol{\varepsilon}(\mathbf{u})) \mathbf{I} + \frac{1}{3} \boldsymbol{\varepsilon}(\mathbf{u}) \mathbf{E}_t \operatorname{tr}^+(\boldsymbol{\varepsilon}(\mathbf{u})) \mathbf{I} + \frac{1}{3} \boldsymbol{\varepsilon}(\mathbf{u}) \mathbf{E}_c \operatorname{tr}^-(\boldsymbol{\varepsilon}(\mathbf{u})) \mathbf{I} \right) \quad (48)$$

After the finite element discretization, the first term is nearly the same as in 1D, i.e of the form  $\mathbf{K}_e \mathbf{u}_e$  on each element (see equation 35) :

$$\mathbf{K}_e = \int_{\Omega_e} \mathbf{B}_e^T(x) : \mathbf{E}_d(\chi_t^{i-1}, \chi_c^{i-1}) : \mathbf{B}_e(x) dx. \quad (49)$$

On each element, the new terms containing the *trace* terms, can be written introducing the generic notation  $\mathbf{T}_e(\mathbf{u}_e)$ . Calculating these terms leads to:

$$\begin{aligned} \mathbf{v}_e^T \mathbf{T}_{d,e}(\mathbf{u}_e) &= -\frac{1}{3} \int_{\Omega_e} \text{tr}(\boldsymbol{\varepsilon}(\mathbf{u}_e)) \boldsymbol{\varepsilon}(\mathbf{v}_e) : \mathbf{E}_d(\chi_t^{i-1}, \chi_c^{i-1}) : \mathbf{I} \, dx \\ &= -\frac{1}{3} \mathbf{v}_e^T \int_{\Omega_e} \text{tr}(\mathbf{B}_e(\mathbf{x}) \mathbf{u}_e) \mathbf{B}_e^T(\mathbf{x}) : \mathbf{E}_d(\chi_t^{i-1}, \chi_c^{i-1}) : \mathbf{I} \, dx \end{aligned} \quad (50)$$

$$\begin{aligned} \mathbf{v}_e^T \mathbf{T}_{t,e}(\mathbf{u}_e) &= \frac{1}{3} \int_{\Omega_e} \text{tr}^+(\boldsymbol{\varepsilon}(\mathbf{u}_e)) \boldsymbol{\varepsilon}(\mathbf{v}_e) : \mathbf{E}_t(\chi_t^{i-1}, \chi_c^{i-1}) : \mathbf{I} \, dx \\ &= \frac{1}{3} \mathbf{v}_e^T \int_{\Omega_e} \text{tr}^+(\mathbf{B}_e(\mathbf{x}) \mathbf{u}_e) \mathbf{B}_e^T(\mathbf{x}) : \mathbf{E}_t(\chi_t^{i-1}, \chi_c^{i-1}) : \mathbf{I} \, dx \end{aligned} \quad (51)$$

$$\begin{aligned} \mathbf{v}_e^T \mathbf{T}_{c,e}(\mathbf{u}_e) &= \frac{1}{3} \int_{\Omega_e} \text{tr}^-(\boldsymbol{\varepsilon}(\mathbf{u}_e)) \boldsymbol{\varepsilon}(\mathbf{v}_e) : \mathbf{E}_c(\chi_t^{i-1}, \chi_c^{i-1}) : \mathbf{I} \, dx \\ &= \frac{1}{3} \mathbf{v}_e^T \int_{\Omega_e} \text{tr}^-(\mathbf{B}_e(\mathbf{x}) \mathbf{u}_e) \mathbf{B}_e^T(\mathbf{x}) : \mathbf{E}_c(\chi_t^{i-1}, \chi_c^{i-1}) : \mathbf{I} \, dx \end{aligned} \quad (52)$$

$$\begin{aligned} &= \frac{1}{3} \mathbf{v}_e^T \int_{\Omega_e} \text{tr}^-(\mathbf{B}_e(\mathbf{x}) \mathbf{u}_e) \mathbf{B}_e^T(\mathbf{x}) : \mathbf{E}_c(\chi_t^{i-1}, \chi_c^{i-1}) : \mathbf{I} \, dx \end{aligned} \quad (53)$$

Finally, from the variational formulation, we drop the  $\mathbf{v}$  function in admissible displacement set, and we get the following non-linear residual to solve for  $\mathbf{u}^i$ :

$$\mathbf{R}(\mathbf{u}) = \sum_{e=1}^N \frac{1}{2} \mathbf{K}_e(\chi_{t,e}^{i-1}, \chi_{c,e}^{i-1}) \mathbf{u}_e + \mathbf{T}_{d,e}(\mathbf{u}_e) + \mathbf{T}_{t,e}(\mathbf{u}_e) + \mathbf{T}_{c,e}(\mathbf{u}_e) - \mathbf{F}_e^i. \quad (54)$$

*Remark:* under the plane-strain hypothesis, we use Voigt formulation and thus all the tensors reduce to 2D matrices. The residual  $\mathbf{R}(\mathbf{u})$  is a nonsmooth function. More precisely it is a piecewise linear function of  $\mathbf{u}$  due to the presence the positive and negative part of the trace. Some care must be taken to solve it with a Newton method, since the Jacobian of the residual is not defined everywhere, but only almost everywhere since it is a Lipschitz continuous function. The solution  $\mathbf{u}^i$  is sought as the limit of the sequence  $\{\mathbf{u}^k\}$  given by semi-smooth Newton technique:

$$\begin{cases} \mathbf{u}^0 = \mathbf{u}^{i-1} \\ \mathbf{H}(\mathbf{u}^k)(\mathbf{u}^{k+1} - \mathbf{u}^k) = -\mathbf{R}(\mathbf{u}^k) \end{cases} \quad (55)$$

where  $\mathbf{H}(\mathbf{u})$  is an element of the generalized Jacobian. From a practical point of view, we consider the following choice for computing the elements of the generalized Jacobian,  $g \in \partial_x(x)^+$  and  $h \in \partial_x(x)^-$ :

$$g = \begin{cases} 0 & \text{if } x \leq 0 \\ 1 & \text{if } x > 0 \end{cases} \quad \text{and } h = \begin{cases} 0 & \text{if } x \geq 0 \\ 1 & \text{if } x < 0. \end{cases} \quad (56)$$

The convergence of the Newton method is based on the comparison of the norm of the residual with respect to a user tolerance.

### Calculus of the damaged state

Given the displacement of the beam at time  $t_i$ , to calculate the damage state at each iteration, we minimize the corresponding energy function as defined in (46) depending on the displacement  $\mathbf{u}^i$ :

$$\mathbf{J}(u, \chi_t, \chi_c) = \sum_{e=1}^N \frac{1}{2} \mathbf{u}_e^T \mathbf{K}_e(\chi_{t,e}, \chi_{c,e}) \mathbf{u}_e + \mathbf{u}_e^T \mathbf{T}_{d,e}(\mathbf{u}_e) + \mathbf{u}_e^T \mathbf{T}_{t,e}(\mathbf{u}_e) + \mathbf{u}_e^T \mathbf{T}_{c,e}(\mathbf{u}_e) + \kappa_t \chi_{t,e} + \kappa_c \chi_{c,e} - \mathbf{u}_e^T \mathbf{F}_e \quad (57)$$

subjected to the constraints:

$$\begin{cases} \chi_t^{i-1} \leq \chi_t^i \leq 1 \\ \chi_c^{i-1} \leq \chi_c^i \leq 1 \\ \mathbf{u}^i \in V_i. \end{cases} \quad (58)$$

This minimization problem is solved with a quasi-Newton method with projection, suited for bound constrained nonlinear optimization problems [Bonnans, 1983].

## 5 A case study on avalanche prevention structures

In this section, the model developed in Section 4.3 is validated and commented on academic experiments (tension, compression, cyclic and bending experiments in Section 5.1.1, and three-point flexural test in Section 5.1.2). In Section 5.2, the interest of this model is demonstrated on the forecast of the onset of damage in avalanche prevention structures made of concrete.

### 5.1 Validation and sensitivity experiments

In this section, some experiments are performed to test the sensitivity of the model to various numerical parameters and validate the global behaviour in tension, compression and bending. For each experiment, the configuration is explained and the loading scenario is detailed. Our goal is to show that the model does not exhibit sensitivity to mesh sizes and loading step sizes. We sum up in Table 2 the general parameters for the validation of the model in 2-D.

| Numerical parameters                   |  |
|--|--|
| Total length of the beam               | $L = 2$ m                              |
| Thickness of the beam                  | $h = 0.1$ m                            |
| Young coefficient for sound concrete   | $E_0 = 2.10^{10}$ Pa                   |
| Young coefficient for damaged concrete | $E_1 = 2.10^9$ Pa                      |
| Damage parameter in traction           | $\kappa_t = 300$ J/m <sup>3</sup>      |
| Damage parameter in compression        | $\kappa_c = 10000000$ J/m <sup>3</sup> |

Table 2: Characteristic parameters of a 2-D beam for numerical illustrations

### 5.1.1 Validation of the model: tension, compression, cyclic and bending experiments

In order to validate our model with tension-compression terms, we perform different numerical test scenarios. First a pure tension or compression simulation allows testing separately the effect of the damage coefficients  $\kappa_c$  and  $\kappa_t$ . Then, a cyclic experiment allows to verify the irreversibility of the phenomenon. Finally a bending test shows the ability of the model to consider mixed damage modes. In each situation, the sensitivity to some numerical parameters (mesh size,  $E_1$  values, initial default, load step size, ...) is tested.

#### Pure tension or compression experiment

A tension force is applied to the superior part of the beam, increasing in time and equally distributed on the upper face of the beam as we can see on the left side in Figure 10. We also observe in Figure 10 that the damage part in compression is null, as expected, and the displacement at the top of the beam is consistent with the applied force, and reveals the two slopes representing the elasticity of the sound and damaged material.

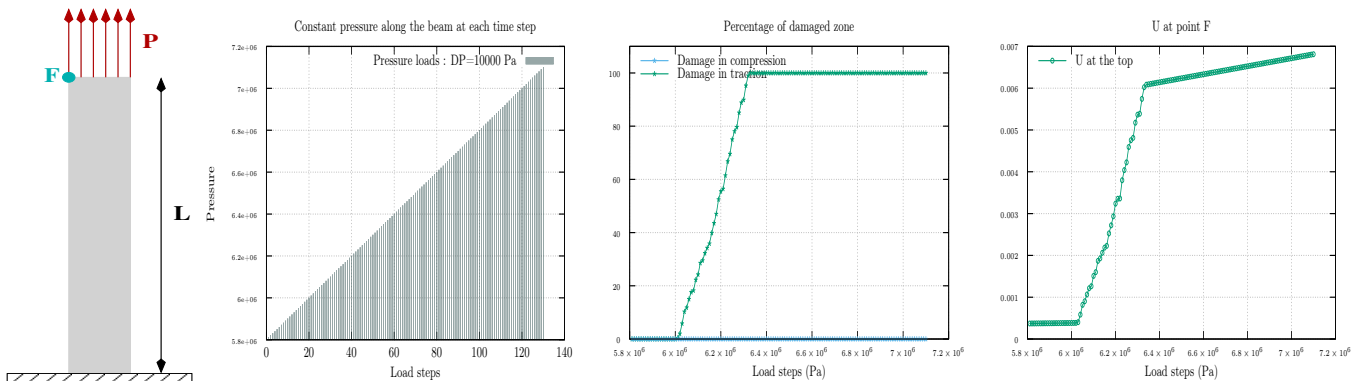


Figure 10: Tension-Compression model: configuration of the tension experiment (left), pressure load (center left), damage function in percentage (center right) and the displacement  $U$  at the F point (right).

In order to analyze the sensitivity of the model to the mesh size, we performed the same experiment with different mesh sizes, and we compare the resulting damage states. We can observe in Figure 11 that if the mesh is too coarse, the critical load for damage is not correctly caught by the model. Increasing slightly the number of elements solves this problem. Above a threshold in the number of elements, the sensitivity of the results to the mesh size is small. We also note that the arrangement of the elements is different from one mesh to another, especially on the boundaries. This explains the small differences between the cases. Finally, for the experiment in the pure tension test, we can remark that no spurious damage in compression appears due to the mesh choice.

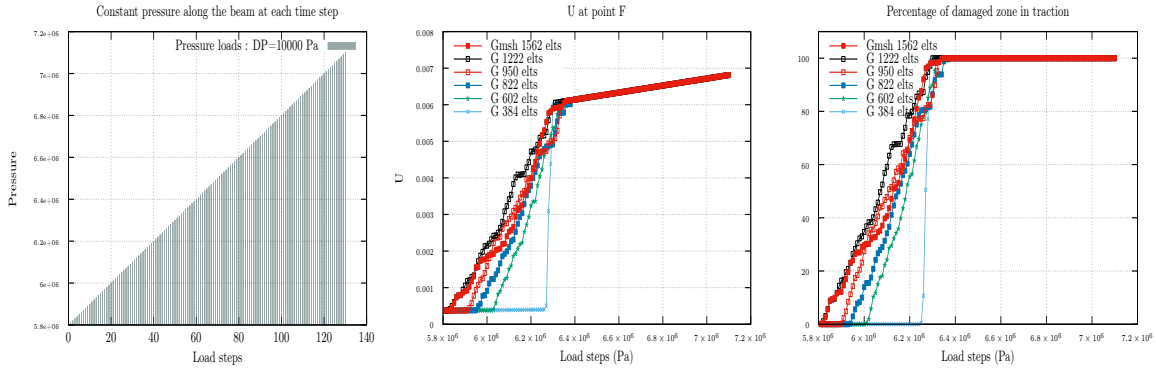


Figure 11: Comparison between different sizes of mesh with constant  $\Delta P = 10000$  Pa: scenario of charge (left), displacement ( $U$ ) at the top point (center) and damage evolution in percentage (right).

Concerning the sensitivity to the load step, in Figure 12, which represents three different load step sizes, we can observe that the evolution of damage is modified. This shows that the damage state depends on the history of loading and also reflects the non-linearity between the exerted force and the resulting damage. Note that the chosen numerical strategy might also have an influence, since, at each loading step, we do not use fixed point iterations between the displacement problem and the damage problem to get convergence.

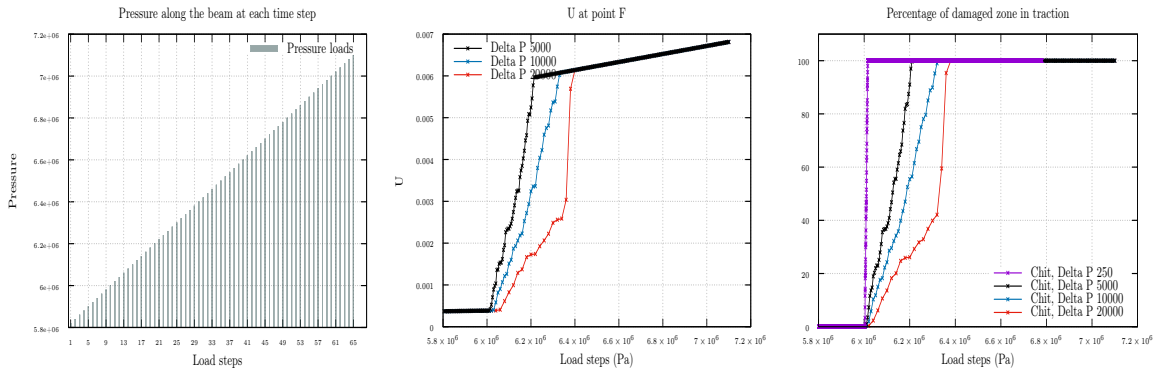


Figure 12: Comparison between different load steps with constant size of grid: scenario of charge (left),  $U$  at the top point (center) and damage evolution (right).

Regarding the compression experiment, we obtain comparatively equivalent results that are not reported in the article for the sake of length.

### Experiments on $E_1$ damage state values (same configuration as in Figure 10)

A fundamental assumption of the model is that  $E_1$  must be positive to preserve the stability of the solution. In the following experiments, we test different values of  $E_1$  from  $2.10^9$  Pa to  $2.10^3$  Pa during a tension experiment. We can observe in Figure 13 that the evolution damage is rather different, which can be explained by the modified law of  $E_d$ ,

and  $E_t$  and  $E_c$  as well. We can see that the critical bound for damage is also different. As it is not so easy to find the numerical value for the Young modulus of damaged concrete, we can note that the global behaviour does not change in shape except for the very small value  $2 \cdot 10^3$  Pa.

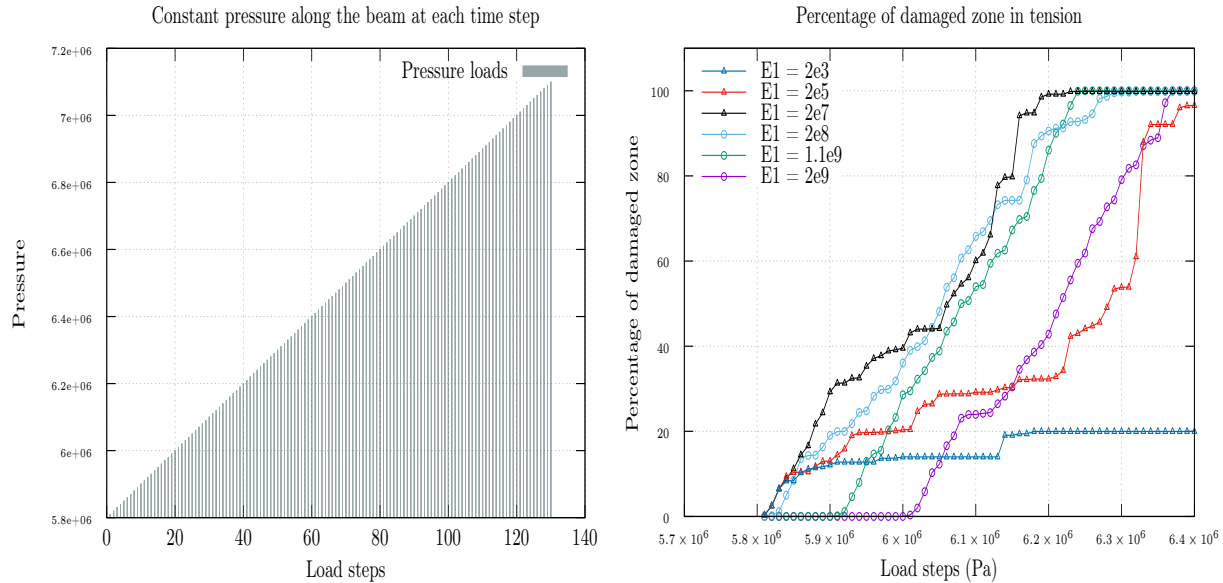


Figure 13:  $P$ ,  $\chi_t$  for the tension experiment with different values of  $E_1$  parameters from  $2 \cdot 10^9$  Pa to  $2 \cdot 10^3$  Pa

### Tensile test with an initial default

With no initial default, the evolution of damage is illustrated in Figure 14 and Figure 15. The onset of damage occurs near the clamped boundary condition. Adding a partially damage element at the center of the beam as an initial default ( $\chi_t = 0.9$ ), the onset of damage is substantially modified. In Figure 16 and 17, we see that the damage zone propagates from the zone of the initial default. In spite of the initial default, the propagation of damage in the structure is very similar with respect to the load (the load scenario is the same as the experiment without initial default, with  $\Delta P = 10000$  Pa). Only the onset of damage is quicker due to the presence of the initial default. We can also observe that at the onset of the damage, we still have a non-negligible level of stress at the basis of the beam. In these experiment, we also calculated the Von Mises norm of the stress, called hereafter VMS.

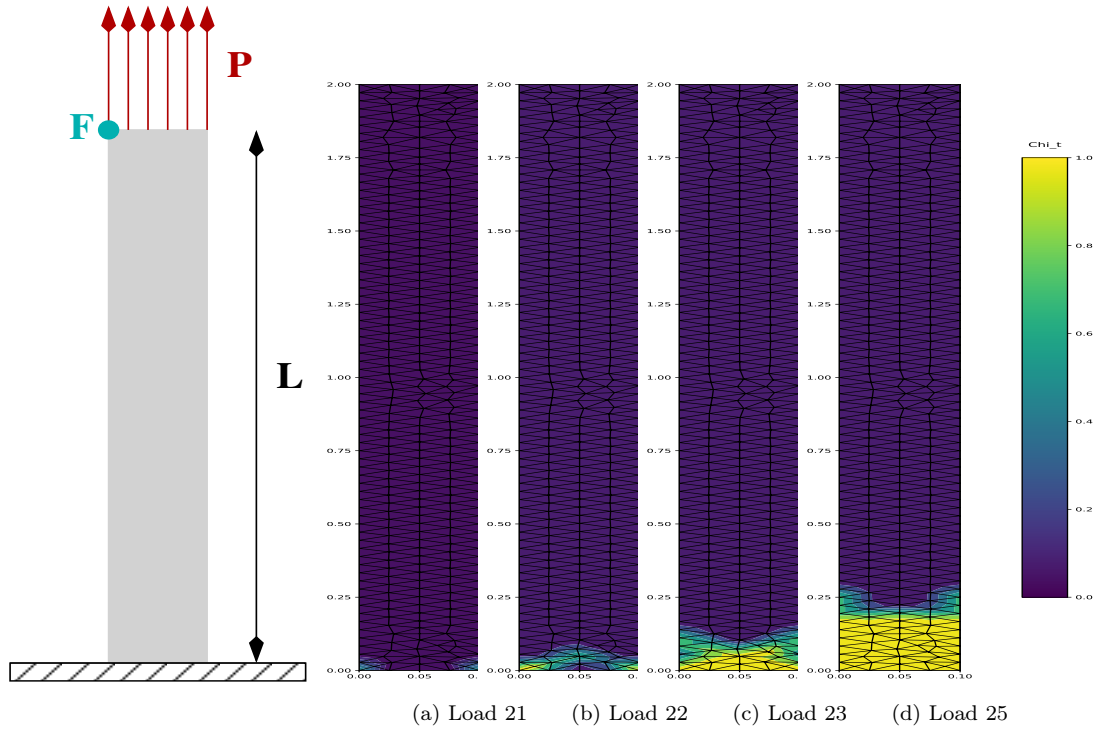


Figure 14:  $\chi_t$  evolution from the first damage state

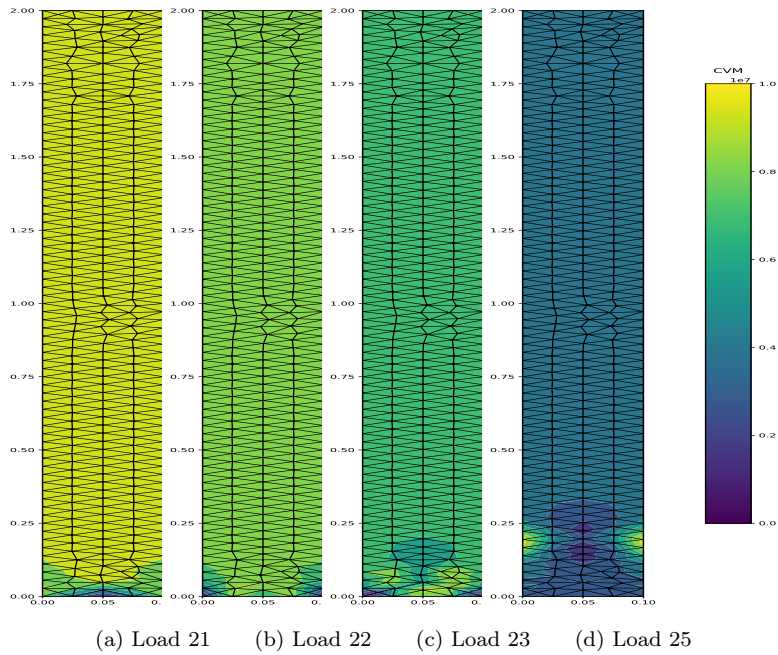


Figure 15: Corresponding VMS evolution during the tensile test without initial default

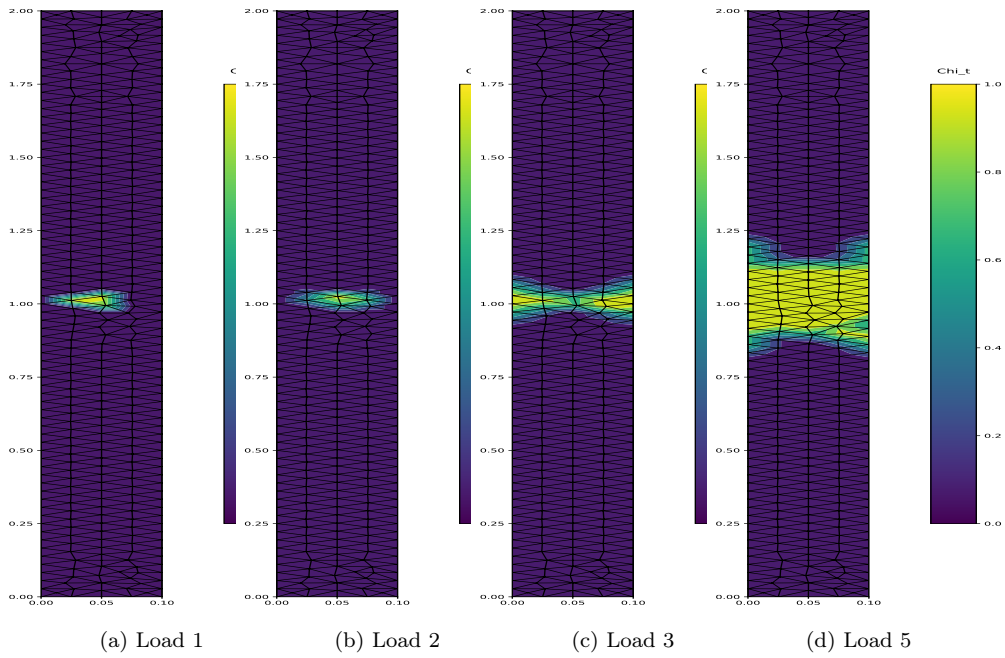


Figure 16:  $\chi_t$  evolution from the first damage state with an initial default

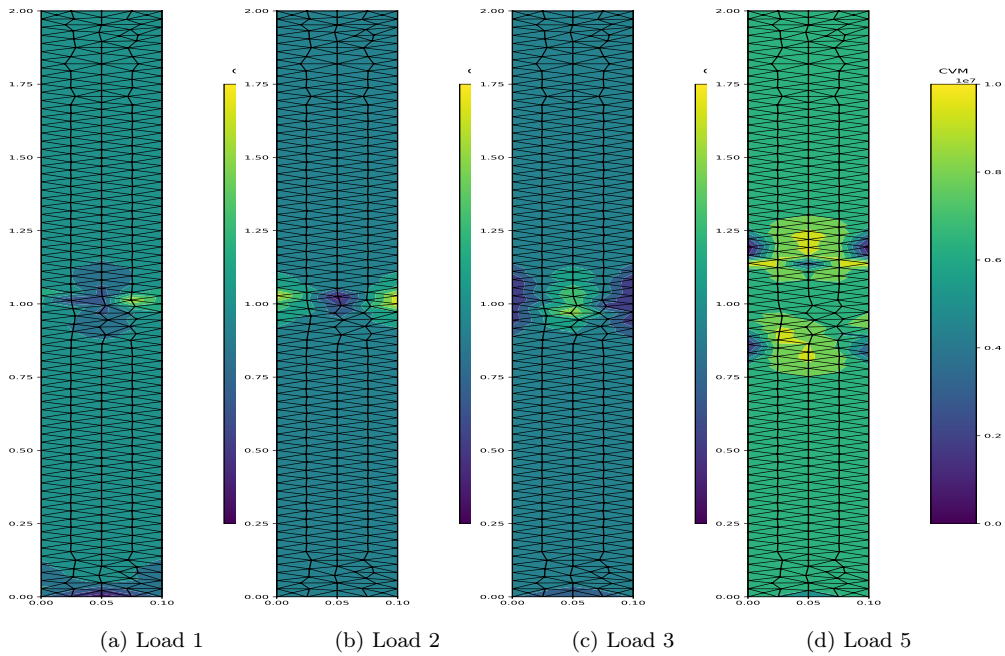


Figure 17: Corresponding VMS evolution during the tensile test with an initial default

### Cyclic experiment with equal threshold values and damage

In this paragraph, we perform here a cyclic experiment (a tension phase followed by a compression phase) with equal

threshold values in tension and compression),  $\kappa_t = \kappa_c = 300$  such that the damage may develop in both directions.

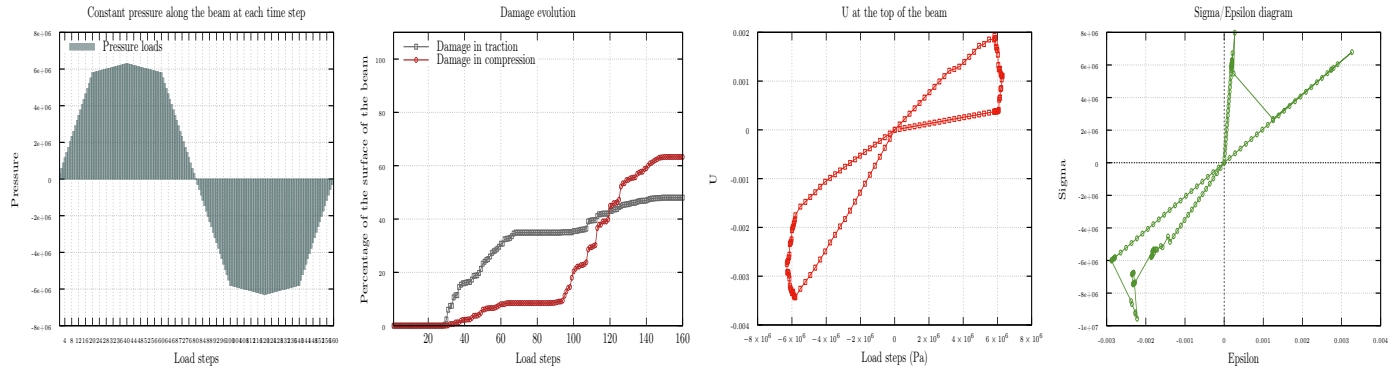


Figure 18: Traction-compression Model: tension-compression cycle. Applied load  $P$ , evolution of damage  $\chi_t$  and  $\chi_c$ , displacement at the top of the beam  $U$  and the stress  $\sigma$  with respect to the strain  $\varepsilon$  (values of  $\sigma$  and  $\varepsilon$  are taken at the central point).

In Figure 18, we see that before ending the tension phase, the damage by compression begins. Moreover, both percentage of final damage are not equal: compression damage percentage is higher, which means that the structure due to its geometry is more sensible to compression. The final value of damage percentage is around 62%. We have to note that the damage in compression occurs in an already damaged structure, which leads to unsymmetrical results.

If we have look at the  $(\sigma, \varepsilon)$  diagram, we can see that the two parts of the cycle are not identical neither the displacement at the top of the beam, as the damage in compression begins before the end of tension phase.

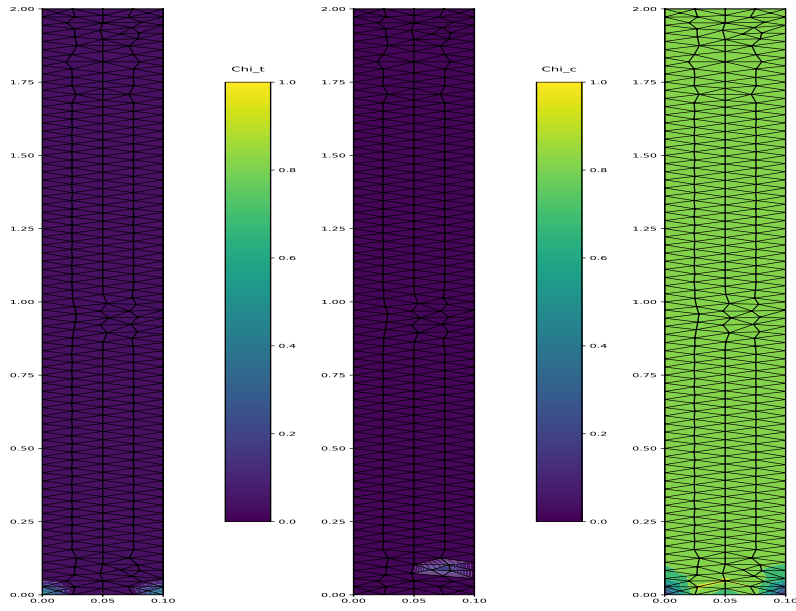


Figure 19: TC Model: tension-compression cycle.  $\chi_t$  at load 29 (left),  $\chi_c$  at load 31 (center) at the onset of the damage and corresponding VMS field (right, load 30).

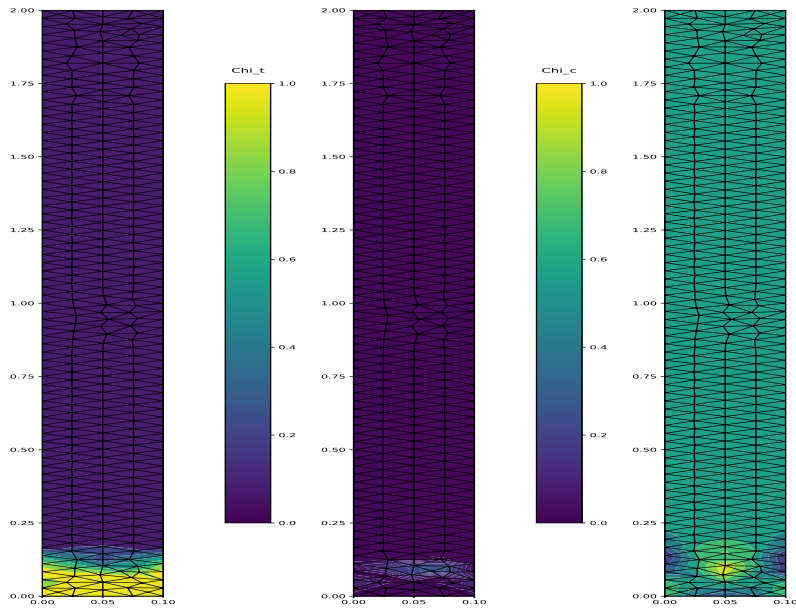


Figure 20: TC Model: tension-compression cycle.  $\chi_t$  (left),  $\chi_c$  (center) and VMS field (right) at load 32.

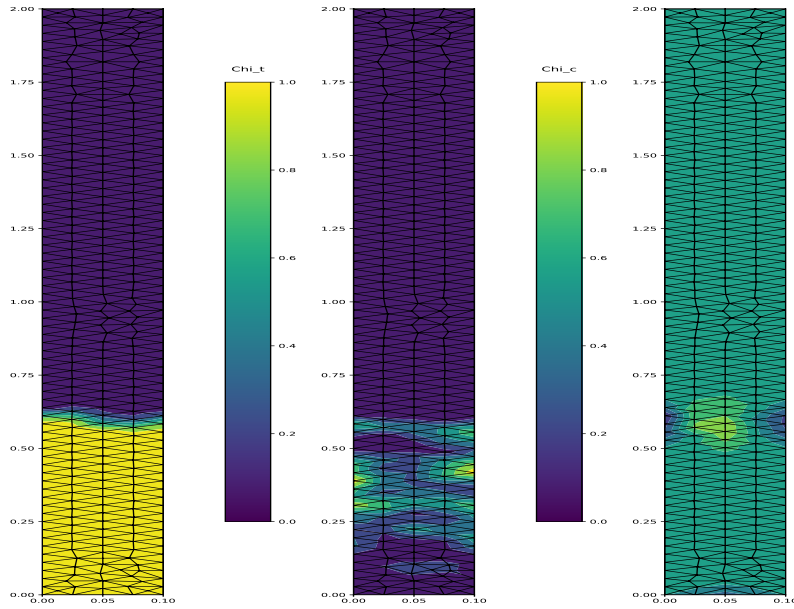


Figure 21: TC Model: tension-compression cycle.  $\chi_t$  (left),  $\chi_c$  (center) and VMS field (right) at load 60.

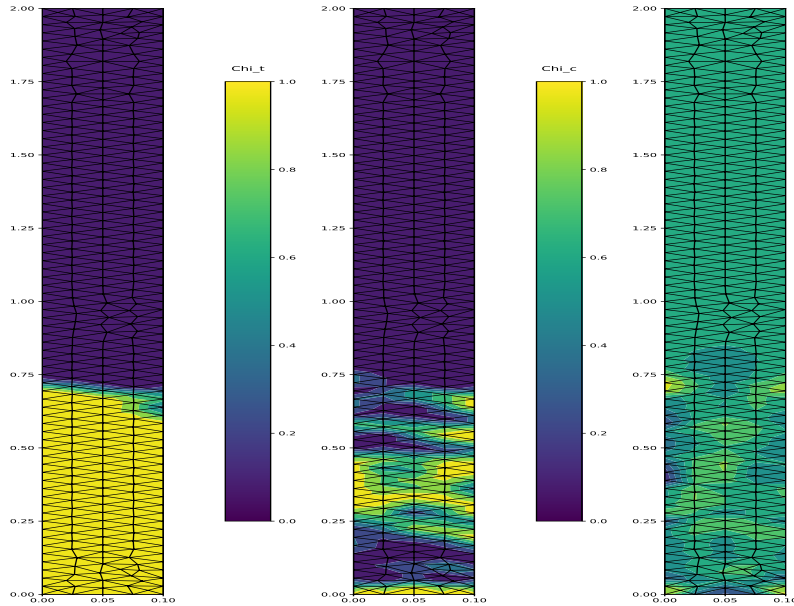


Figure 22: TC Model: tension-compression cycle.  $\chi_t$  (left),  $\chi_c$  (center) and VMS field (right) at load 99.

The damage in tension propagates from the bottom towards the top of the beam, in nearly continuous manner. Contrary to that, the damage in compression presents a different spatial distribution, with layers of damaged and undamaged areas. In the last Figure 22, the damage state slowly evolves, showing the vertical propagation of the damage in tension and the localized damage in compression.

To compare we perform another cycle experiment, but we begin with the compression phase as we will see below.

### Reverse cyclic experiment with equal threshold values

In this experiment, we begin with the compression phase and we can see that the resulting compression damage rate is higher at the beginning of the experiment (Figure 23). At the end, contrary to the previous experiment, the final damage rate in tension is higher. We have to notice that the final value of the damage is around 50% in this experiment.

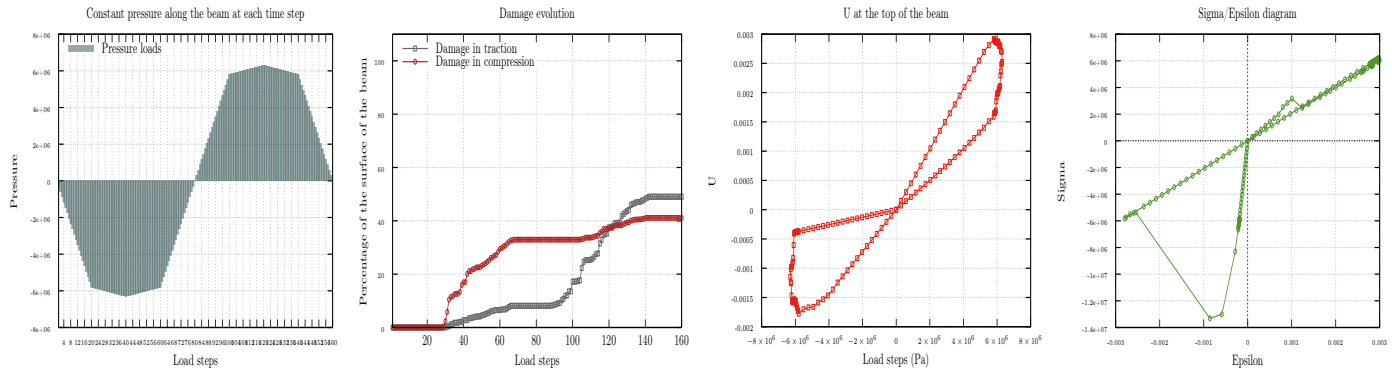


Figure 23: TC Model: tension-compression cycle.  $P$ ,  $\chi$ ,  $U$  et  $\sigma/\varepsilon$  (values of  $\sigma$  and  $\varepsilon$  are taken at the central point).

The difference between the two experiments can be explained by the geometry of the beam. In these examples, the beam is thin compared to its length. Therefore, when the compression phase occurs, the transverse efforts are supported by the very thin part of the beam, while the tension effort tends to contract the structure. We also can observe as a consequence that the  $(\sigma, \varepsilon)$  diagram is also slightly different.

### Cyclic experiment with realistic threshold values

We perform here a cyclic experiment (a tension phase followed by an equivalent compression phase) with differentiated threshold values in tension and compression (See table 2).

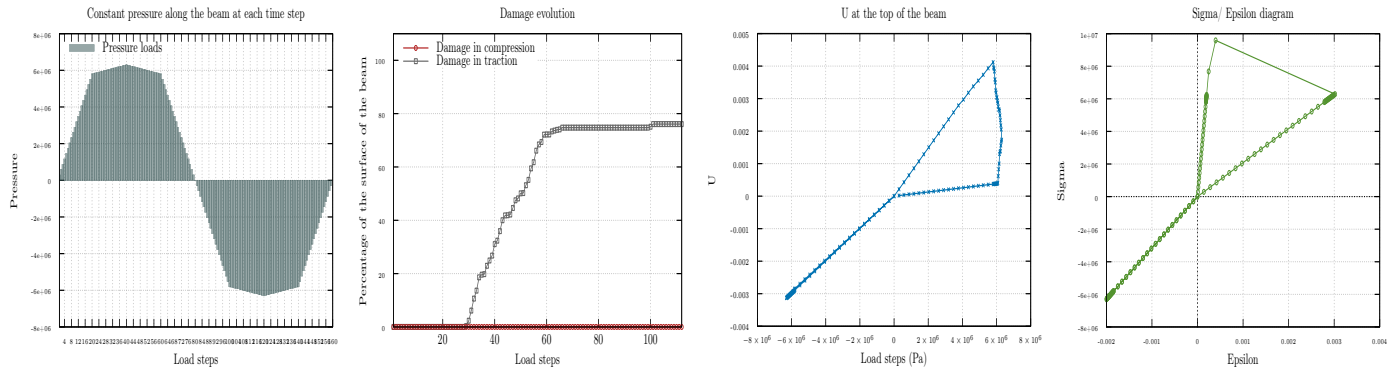


Figure 24: TC Model: tension-compression cycle.  $P$ ,  $\chi$ ,  $U$  and  $\sigma/\epsilon$ , for  $E_1 = 2.10^9$  Pa (values of  $\sigma$  and  $\epsilon$  are taken at the central point)

We can see in Figure 24, that as the threshold values are very different, mimicking real concrete materials, the resulting damage state in compression remains null. We also note that the damage state in tension never decreases even during compression phase, showing the irreversibility of the process.

Finally, we can see on the  $\sigma/\epsilon$  diagram the consequence of the damage on the upper part of the figure (change of the elasticity slope) and the undamaged behaviour in compression in the lower part of the figure. We can observe that the slope during the compression part without damage is not equal to the slope of the tension part without damage; It is mainly due to the fact that the displacement  $\epsilon_{11}$  (transverse part) is not null during the compression phase as we can see in Figure 25 (that means that the transversal efforts are not null) and the damage function has been modified during the tension part of the experiment.

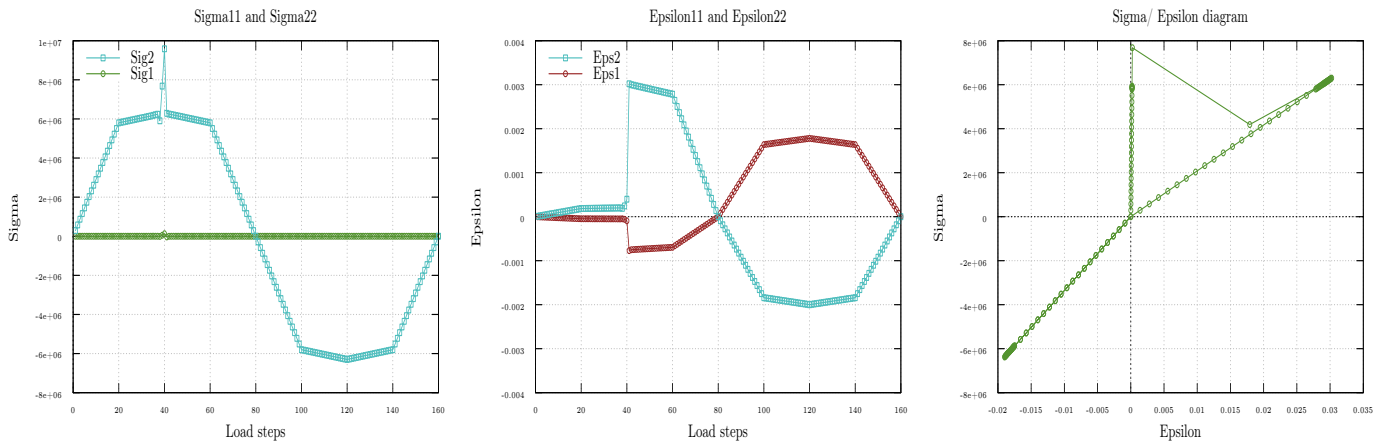


Figure 25: TC Model: tension-compression cycle. Evolution of  $\sigma_{11}$ ,  $\sigma_{22}$  (left),  $\epsilon_{11}$  and  $\epsilon_{22}$  during the loads (center),  $\sigma/\epsilon$  for  $E_1 = 2.10^8$  Pa (right) (values of  $\sigma$  and  $\epsilon$  are taken at the central point).

We can observe in Figure 25 that decreasing the value of  $E_1$  in the cyclic experiment, on one hand increases the

value of stress and strain during the tension phase (horizontal scale is not the same) but not affect the compression phase.

### Bending experiment with realistic threshold values

In this part we perform a real bending experiment. The force is applied on the left face of the beam and is for the moment spatially constant along the face, but varying in intensity with time ( $\Delta P = 500$  Pa).

First, we can note that due to high threshold value in compression, no damage appears in that direction. On the other hand, we can see in Figure 26 that the percentage of total damage in tension slightly varies with the mesh size. The most varying quantity is the displacement at the top of the beam at the end of the experiment: it is due to the position of the elements in the unstructured mesh.

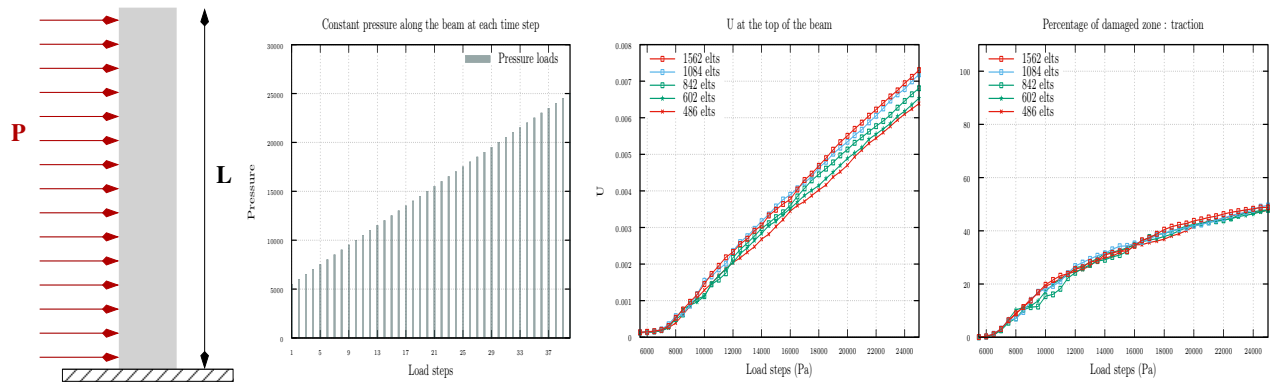


Figure 26: Comparison of different mesh size

We made some tests concerning the damage threshold in compression in this bending configuration. As expected, the more the threshold increases the more the percentage of the damage zone decreases. We can also state from these results that the modifications of the damage zone in compression does not affect the damage part in tension (see Figure 27).

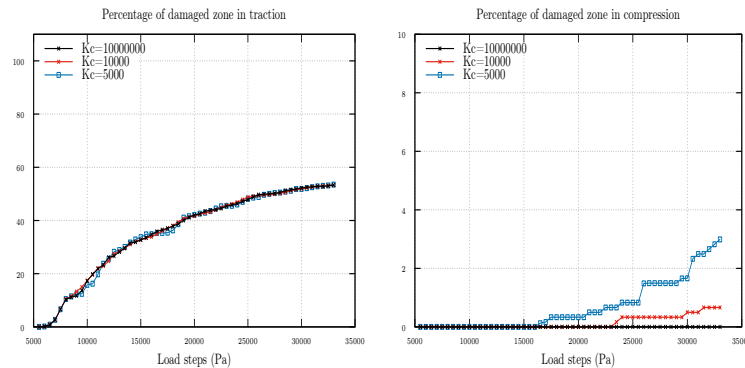


Figure 27: Damage in tension (left) and in compression (right) for different values of the threshold in compression.

### 5.1.2 Three-point flexural test

This experiment is a classical three-point flexural test. Figure 28 presents the complete configuration and the axis of symmetry. The black triangles represent the support. The initial default is located along the blue vertical line on half of the total height of the beam (no U-notch or V-notch surface). Thanks to the symmetry of the problem, we solve half of the configuration with symmetric boundary conditions.

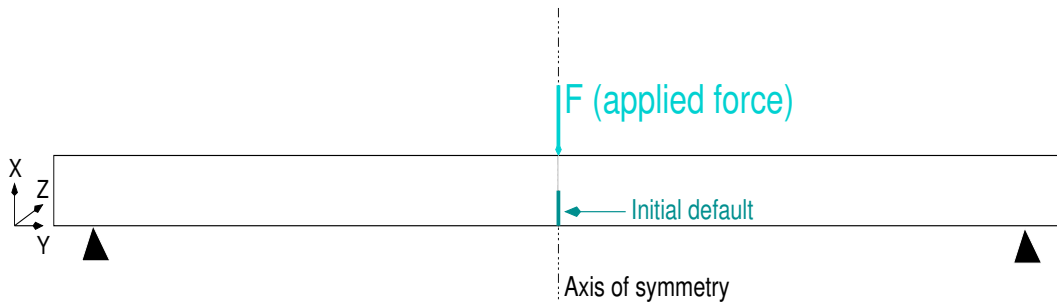


Figure 28: Configuration of the three-point flexural experiment

Due to the high threshold in compression, no damage in compression is observed in this experiment (Figure 29 and Figure 30). The damage in tension is initiated at first free point, in the middle of the beam. No initial default is integrated in the structure but only a virtual crack in the lower center of the beam. The damaged area then propagates up along the vertical as we can see on figure (31), leading to the complete break of the beam.

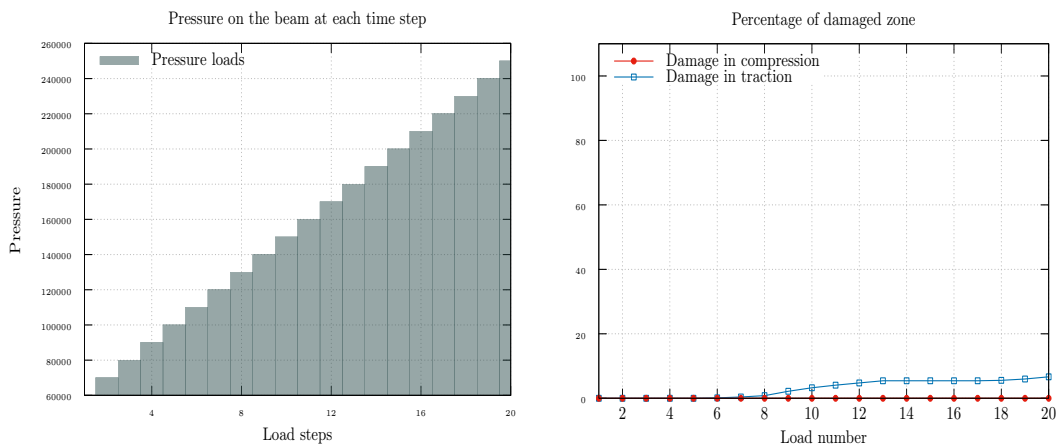


Figure 29: Load scenario and Damage fields

Initiation of the damage is associated with high VMS value in the same area as we can see on figure (30).

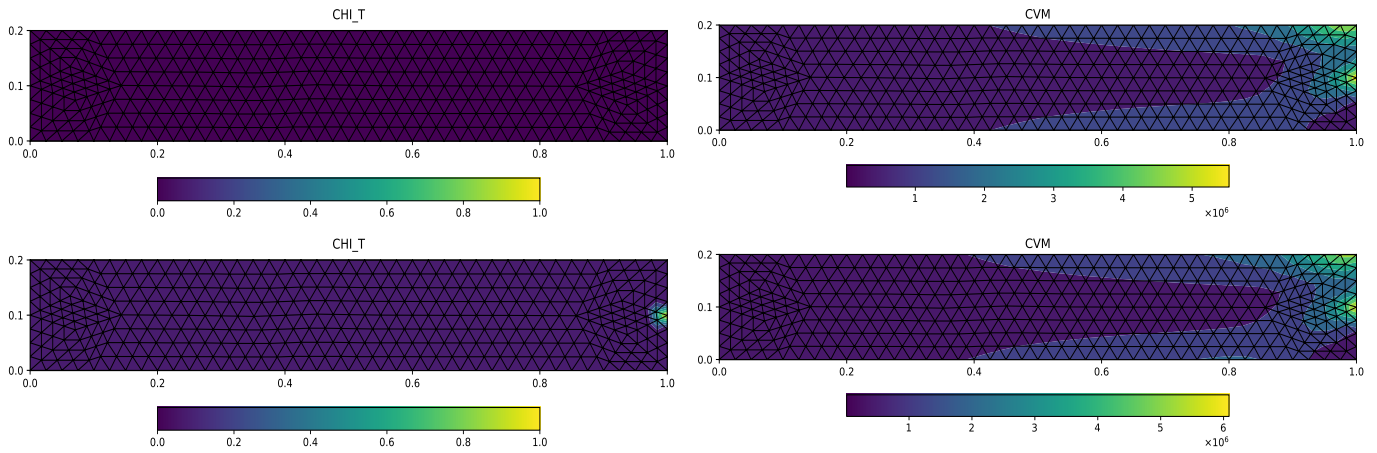


Figure 30:  $\chi$  in tension (left) and VMS (right) fields at the onset of the damage

Then, when the damage is propagating up along the vertical boundary, VMS values seem to decrease in the center, where the stress is relaxed.

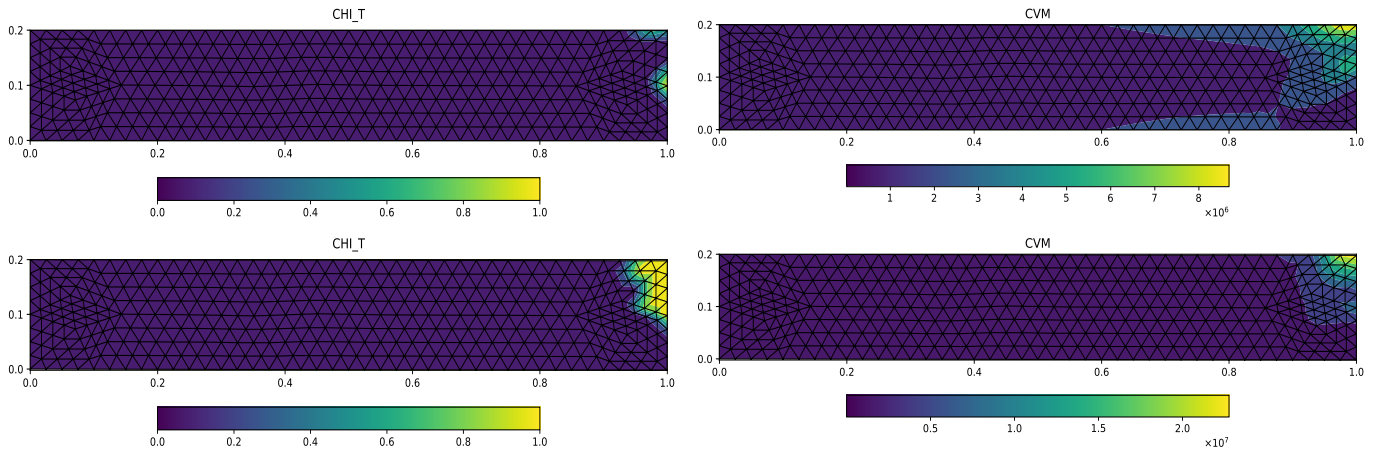


Figure 31:  $\chi$  in tension (left) and VMS (right) fields during the propagation of the damage

In this last figure (32), we show the displacement of the mesh magnified by a factor 10. We can see that as expected the beam is moved down under the force effect, while the support point keeps its original location.

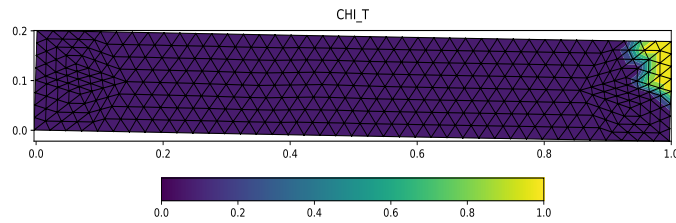
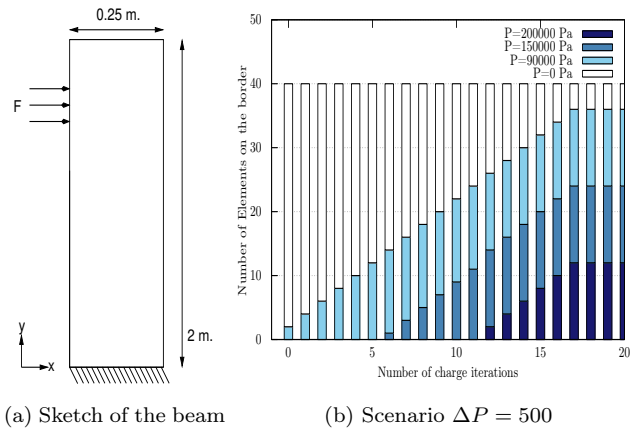


Figure 32:  $\chi$  in tension fields with the grid x10

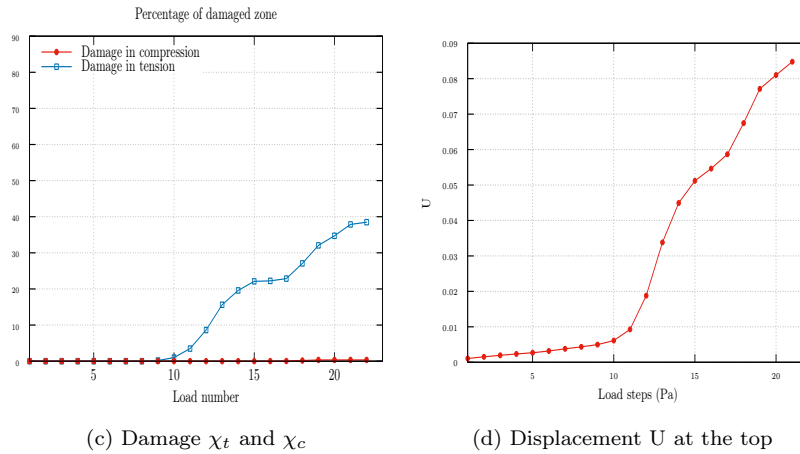
As a conclusion, we can say that through various semi-realistic experiments, we have shown that the model is able to reproduce the main characteristics of a tension-compression damage model. Neither excessive sensitivity nor spurious behaviour related to the numerical parameters of the simulation such as grid size, and the history of loading have been noticed. We propose now to test the model in a realistic scenario of falling dense avalanche with 3 densities of snow, in a pure flexural experiment.

## 5.2 Realistic configuration

In this configuration, the snow is composed of three different density layers and does not reach all the height of the beam. The size of the beam is slightly different because we take a greater dimension in the horizontal direction. The exerted pressure is distributed up to a prescribed height of the structure as we can see in Figure 33b. The pressure values and profile are realistic ones as given, for example, in [Sovilla et al., 2008] or in [Sovilla et al., 2016].



(a) Sketch of the beam (b) Scenario  $\Delta P = 500$



(c) Damage  $\chi_t$  and  $\chi_c$  (d) Displacement  $U$  at the top

Figure 33: Load schemes and damage zone of the beam

At the onset of the damage in tension, we can observe that the VMS values of stress are symmetrically located on both vertical faces of the beam and are maximum just before the damage occurs. Moreover, we can see that damage in tension appears on both faces (Figure 34).

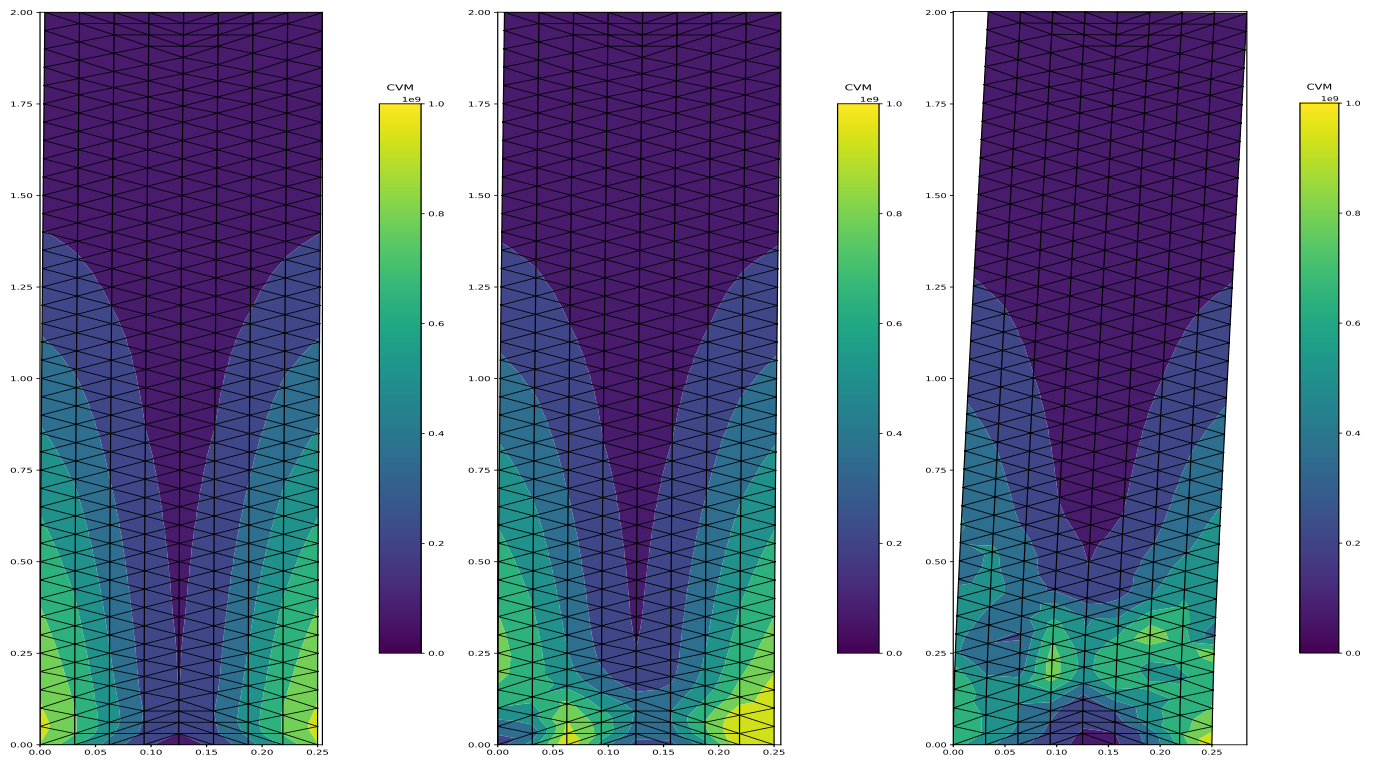


Figure 34: VMS stress at loads 9, 11 and 14

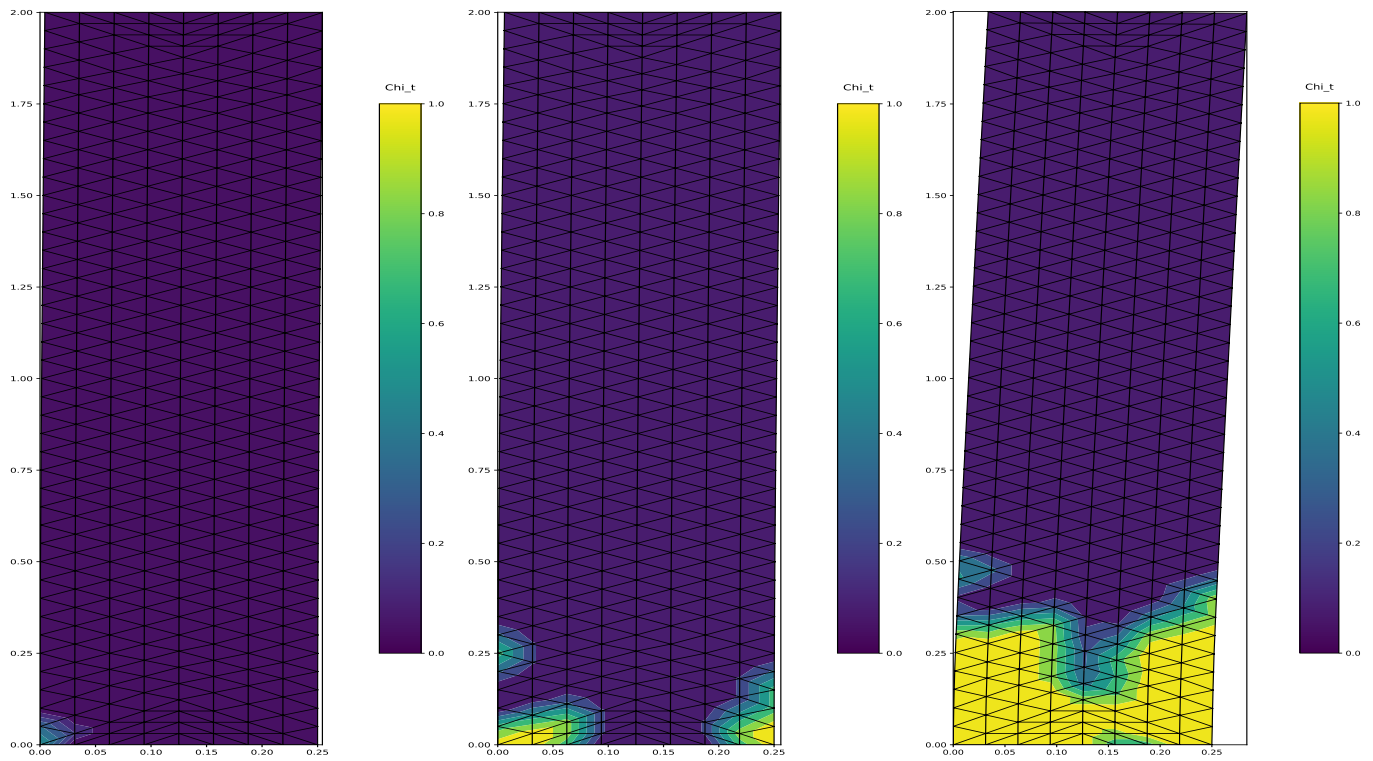


Figure 35: Damage area in tension:  $\chi_t$  field at loads 9, 11 and 14

Regarding the onset of the damage in compression, we can see in Figure 36 and Figure 37 that the onset of damage in compression occurs later, due to the difference in the threshold value of damage. We can also see that the VMS stress is greater on the right face, where the damage in compression occurs in this experiment, although the maximum value is lower than the damage in tension occurs. Contrary to damage in tension, no damage is observed on the opposite face (on the left).

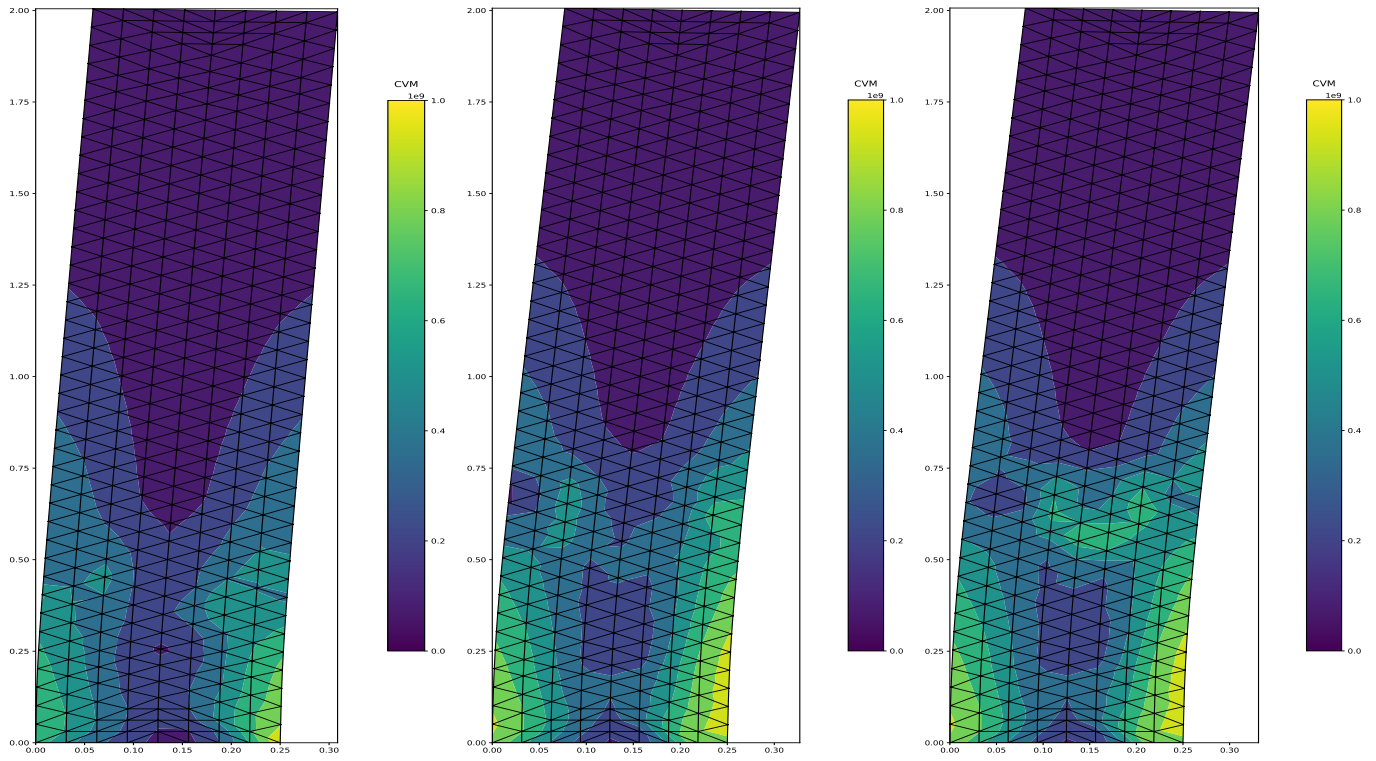


Figure 36: VMS stress at loads 18, 20 and 21

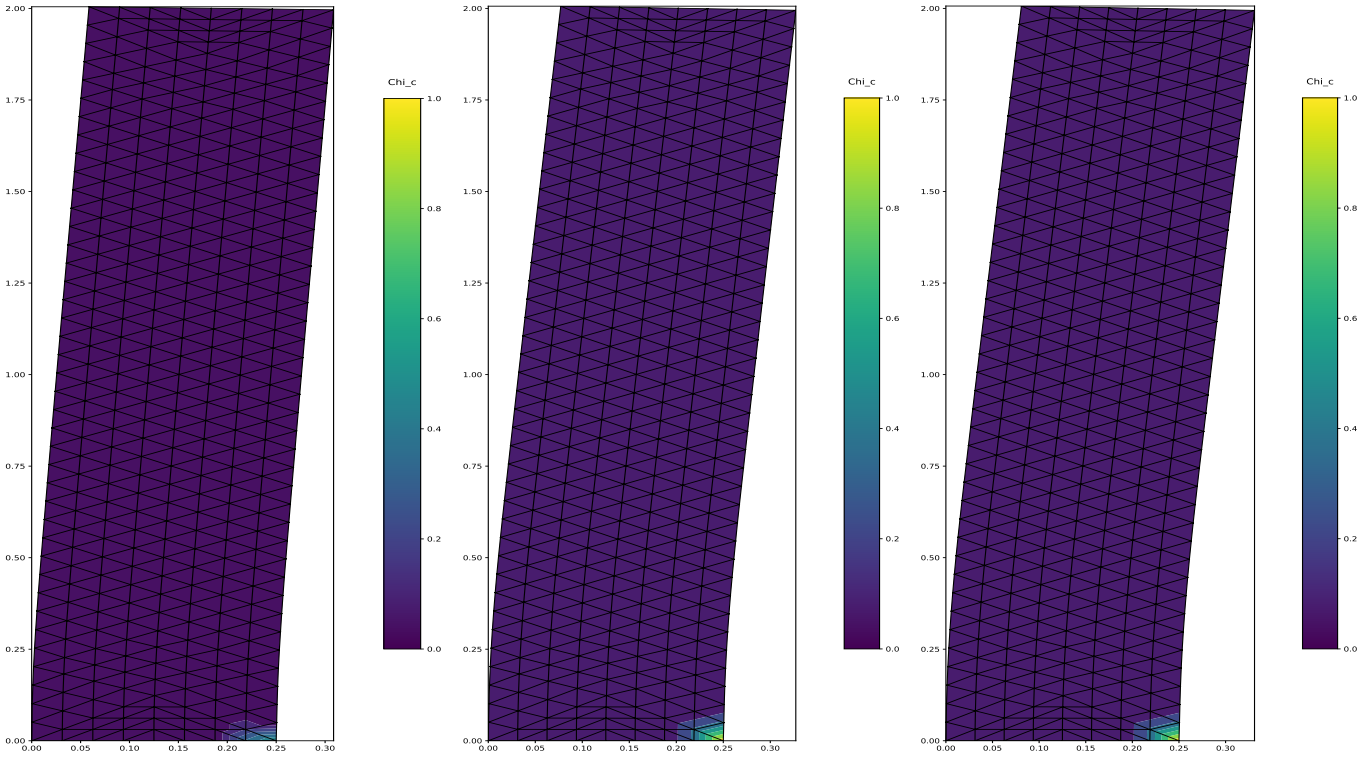


Figure 37: Damage area in compression:  $\chi_t$  field at loads 18, 20 and 21

## Discussions

In this experiment the numerical parameters have been chosen to be close to the real situation. In so far as each real situation has its own characteristics, we choose on special configuration and scenario of avalanche to probe our model. This experiment shows us that the model is able to reproduce in a realistic way the effects of a three-layers dense avalanche with various scenarios. The difference between damage in tension and compression is correctly reproduced in the expected areas. Moreover, this can be easily adapted to other geometries and other load scenarios.

## 6 Conclusion

In this article, a mechanical model of damage which considers a different behavior in traction and in compression is developed in the framework of a variational approach to damage pioneered by Francfort & Marigo. A numerical method for this mechanical model is also proposed based on the minimization of the total energy, by alternating the minimization on the displacements and on the damage variables. Beyond the development of the model and the numerical method, the main achievements detailed in this article are:

- In the one-dimensional (1-D) setting, analytical developments have been carried out to give closed-form formulae of the limit pressure that causes the onset of damage. A sequence of 1-D experiments validates our model, and

---

we analyze its mathematical and numerical properties such as convergence and sensitivity to parameters. We have shown that our numerical approach was in good agreement with the analytical results.

- In the two-dimensional (2-D) setting, the numerical experiments demonstrated good properties with respect to the sensitivity to numerical parameters. They have shown good agreement with what was expected, *i.e.* a low sensitivity to the grid size and a good behavior during charge and discharge cycles. Furthermore, the model was able to reproduce the main expected features of the damage evolution related to the introduction of tension-compression terms. Naturally, the results depend on the critical parameters of the model such as the history of loads, the geometry and the Young modulus, but in a coherent way. In several standard mechanical configurations, such as a tension/compression cycle and a three-point flexural test, the resulting solutions are in good agreement regards to the literature. The three-point flexural test shows that the numerical method succeeds in finding the initial damage point. In the traction test on the beam, the initiation of the propagation of damage is also well reproduced in the experiment with an initial default.
- Finally, realistic experiments have been performed to analyze the response of a concrete structure to avalanche impacts.

As a conclusion, we can stat that the model shows its interest for forecasting the structural safety of concrete protection walls

As a perspective to this work, the following items can be listed:

- The numerical method needs to be implemented in a High-Performance Computing (HPC) context to enable the simulation of large 3-D structures. Our implementation is quite time-consuming, the Fenics environment as used in [Tanné et al., 2018] could be a good option.
- The quasi-static formulation limits our study to the cases of slow dense avalanches. To consider high-speed powder-snow avalanches, the introduction of the dynamics is mandatory.

Finally, we can state that our model meets the objectives that have been laid down, that is, to forecast accurately the onset of damage in a concrete structure. With a quite manageable and user-friendly code, the model is able to determine the main zones of damage due to an impact of a dense avalanche.

## References

- [Alberty et al., 2002] Alberty, J., Carstensen, C., Funken, S., and Klose, R. (2002). Matlab implementation of the finite element method in elasticity. *Computing*, 69(3):239–263.
- [Alfaiate and Sluys, 2017] Alfaiate, J. and Sluys, L. J. (2017). On the modelling of mixed-mode discrete fracture: Part i – damage models. *Engineering Fracture Mechanics*, 182(3):157–186.

- 
- [Allaire et al., 1998] Allaire, G., Aubry, S., and Jouve, F. (1998). Simulation numérique de l’endommagement à l’aide du modèle Francfort-Marigo, in Actes du 29ième congrès d’analyse numérique. *ESAIM Proceedings*, 3:1–9.
- [Allaire et al., 2007] Allaire, G., Jouve, F., and Van Goethem, N. (2007). A level set method for the numerical simulation of damage evolution. *Proceedings of ICIAM*, pages 3–22.
- [Ancey et al., 2006] Ancey, C., Bain, V., Bardou, E., Borrel, G., Burnet, R., Jarry, F., Kolbl, O., and Meunier, M. (2006). *Dynamique des avalanches*. Presses polytechniques et universitaires romandes (Lausanne, Suisse).
- [Basov, 2005] Basov, I. V. (2005). Existence of a rigid core in the flow of a compressible bingham fluid under the action of a homogeneous force. *J. math. fluid mech.*, 7:515–528.
- [Beghin and Closet, 1990] Beghin, P. and Closet, J.-F. (1990). Effet d’une digue sur l’écoulement d’une avalanche poudreuse. Technical report, Cemagref.
- [Beghin and Olagne, 1991] Beghin, P. and Olagne, X. (1991). Experimental and theoretical study of the dynamics of powder snow avalanches. *Cold Regions Science and Technology*, 19:317–326.
- [Benallal and Comi, 2005] Benallal, A. and Comi, C. (2005). On interfacial properties in gradient damaging continua. *Comptes Rendus Mécanique*, 334(4):319–324.
- [Bernard et al., 2012] Bernard, P., Moës, N., and Chevaugeon, N. (2012). Damage growth modeling using the thick level set (tls) approach: Efficient discretization for quasi-static loadings. *Computer Methods in Applied Mechanics and Engineering*, 233-236:11 – 27.
- [Berthet-Rambaud, 2004] Berthet-Rambaud, P. (2004). *Structures rigides soumises aux avalanches et chutes de blocs: modélisation du comportement mécanique et caractérisation de l’interaction "phénomène-ouvrage"*. PhD thesis, Université Joseph Fourier.
- [Berthet-Rambaud et al., 2008] Berthet-Rambaud, P., Liman, A., Baroudi, D., Thibert, E., and J.-M., T. (2008). Characterization of avalanche loading on impacted structures: a new approach based on inverse analysis. *J. Glaciol.*, 54(185):324–332.
- [Bertrand et al., 2010] Bertrand, D., Naaim, M., and Brun, M. (2010). Physical vulnerability of reinforced concrete buildings impacted by snow avalanches. *Nat. Hazards Earth Syst. Sci.*, 10:1531–1545.
- [Bleyer and Alessi, 2018] Bleyer, J. and Alessi, R. (2018). Phase-field modeling of anisotropic brittle fracture including several damage mechanisms. *Computer Methods in Applied Mechanics and Engineering*, 336:213 – 236.
- [Bonnans, 1983] Bonnans, F. (1983). A variant of a projected variable metric method for bound constrained optimization problems. *Rapport de recherche de l’INRIA - Rocquencourt*, RR-0242.

- 
- [Bourdin, 1998] Bourdin, B. (1998). *Une Méthode variationnelle en mécanique de la rupture*. PhD thesis, Université Paris 13.
- [Bourdin et al., 2000] Bourdin, B., Francfort, G., and Marigo, J.-J. (2000). Numerical experiments in revisited brittle fracture. *J. Mech. Phys. Solids*, 48:797–826.
- [Bui et al., 1981] Bui, D., Dang Van, K., and Stolz, C. (1981). Formulations variationnelles du problème en vitesse pour le solide élastique-fragile avec zone endommagée. *C. R. Acad. Sc. Paris*, 292(3):125–144.
- [Chambard, 2009] Chambard, M. (2009). *Endommagement anisotrope et comportement dynamique des structures en béton armé jusqu’à la ruine*. PhD thesis, Ecole normale supérieure de Cachan.
- [Comi, 2001] Comi, C. (2001). A non-local model with tension and compression damage mechanisms. *European Journal of Mechanics-A/Solids*, 20(1).
- [Comi and Perego, 2001] Comi, C. and Perego, U. (2001). Fracture energy based bi-dissipative damage model for concrete. *International journal of solids and structures*, 38(36-37).
- [Dutykh et al., 2011] Dutykh, D., Acary-Robert, C., and Bresch, D. (2011). Numerical simulation of powder-snow avalanche interaction with an obstacle. *Studies in Applied Mathematics*, 126(4).
- [Eglit, 1991] Eglit, M. (1991). The dynamics of snow avalanches. In *Proceedings of the Steklov Institute of Mathematics*, volume 186, pages 187–193.
- [Felippa, 2004a] Felippa, C. A. (2004a). *Introduction to Finite elements methods*. Boulder, University of Colorado.
- [Felippa, 2004b] Felippa, C. A. (2004b). *Introduction to Finite elements methods*. Boulder, University of Colorado.
- [Francfort and Garoni, 2006] Francfort, G. and Garoni, A. (2006). A variational view of partial brittle damage evolution. *Archive for Rational Mechanics and Analysis*, 182(1):125–152.
- [Francfort and Marigo, 1991] Francfort, G. and Marigo, J.-J. (1991). Mathematical analysis of the damage evolution in a brittle damaging continuous medium. *Mécanique, modélisation numérique et dynamique des matériaux, Publications du L.M.A., Presses du C.N.R.S.*, 124:245–276.
- [Francfort and Marigo, 1993] Francfort, G. and Marigo, J.-J. (1993). Stable damage evolution in a brittle continuous medium. *Eur. J. Mech., A/Solids*, 12(2):149–189.
- [Francfort and Marigo, 1998] Francfort, G. and Marigo, J.-J. (1998). Revisiting brittle fracture as an energy minimization problem. *J. Mech. Phys. Solids*, 46(8):1319–1342.
- [Frémond and Nedjar, 1996] Frémond, M. and Nedjar, B. (1996). Damage, gradient of damage and principle of virtual power. *Int. J. Solids Structures*, 33(8):1083–1103.

- 
- [Le et al., 2018] Le, D. T., Marigo, J.-J., Maurini, C., and Vidoli, S. (2018). Strain-gradient vs damage-gradient regularizations of softening damage models. *Computer Methods in Applied Mechanics and Engineering*, 340:424 – 450.
- [Lemaitre, 2001] Lemaitre, J., editor (2001). *Copyright*. Academic Press.
- [Lorentz, 1999] Lorentz, E. (1999). *Lois de comportement à gradients de variables internes: construction, formulation variationnelle et mise en œuvre numérique*. PhD thesis, Ecole normale supérieure de Cachan, Université de Paris 6.
- [Lorentz and Andrieux, 2003] Lorentz, E. and Andrieux, S. (2003). Analysis of non-local models through energetic formulations. *International Journal of Solids and Structures*, 40(12):2905–2936.
- [Lorentz and Benallal, 2005] Lorentz, E. and Benallal, A. (2005). Gradient constitutive relations: numerical aspects and application to gradient damage. *Comput. Methods Appl. Mech. Engrg.*, 194:5191–5220.
- [Lorentz and Godard, 2011] Lorentz, E. and Godard, V. (2011). Gradient damage models: Toward full-scale computations. *Computer Methods in Applied Mechanics and Engineering*, 200:1927–1944.
- [Luege et al., 2018] Luege, M., Orlando, A., Almenar, M. E., and Pilotta, E. A. (2018). An energetic formulation of a gradient damage model for concrete and its numerical implementation. *International Journal of Solids and Structures*, 155:160 – 184.
- [Mardare, 2011] Mardare, C. (2011). A nonlinear korn inequality with boundary conditions and its relation to the existence of minimizers in nonlinear elasticity. *C. R. Acad. Sci. Paris, Ser. I*, 349:229–232.
- [Mazars and Pijaudier-Cabot, 1989] Mazars, J. and Pijaudier-Cabot (1989). Continuum damage theory – application to concrete. *J. Eng. Mech.*, 115(2):345–365.
- [Mazars et al., 1991] Mazars, J., Pijaudier-Cabot, G., and Saouridis, C. (1991). Size effect and continuous damage in cementitious materials. *Int. J. Fracture*, 51:159–173.
- [Miehe et al., 2010a] Miehe, C., Hofacker, M., and Welschinger, F. (2010a). A phase field model for rate-independent crack propagation: Robust algorithmic implementation based on operator splits. *Computer Methods in Applied Mechanics and Engineering*, 199(45):2765 – 2778.
- [Miehe et al., 2010b] Miehe, C., Welschinger, F., and Hofacker, M. (2010b). Thermodynamically consistent phase-field models of fracture: Variational principles and multi-field fe implementations. *Int. J. Numer. Meth. Engng*, 83:1273–1311.
- [Naaïm-Bouvet et al., 2002] Naaïm-Bouvet, F., Naaïm, M., Bacher, M., and Heiligenstein, L. (2002). Physical modelling of the interaction between powder avalanches and defence structures. *Nat. Hazards Earth Syst. Sci.*, 2:193–202.

---

[Naaïm-Bouvet et al., 2003] Naaïm-Bouvet, F., Pain, S., Naaïm, M., and Faug, T. (2003). Numerical and physical modelling of the effect of dam on powder avalanche motion: Comparison with previous approaches. *Surveys in Geophysics*, 24 (5/6):479–498.

[Peerlings et al., 1996] Peerlings, R., De Borst, R., W.A.M., B., J.H.P., D. V., and I., S. (1996). Some observations on localisation in non-local and gradient damage models. *Eur. J. Mech., A/Solids*, 15(6):937–953.

[Pham and Marigo, 2010] Pham, K. and Marigo, J.-J. (2010). The variationnal approach to damage: I. the foundations. *C. R. Mecanique*, 2338:191–198.

[Pijaudier-Cabot and Bazant, 1987] Pijaudier-Cabot, G. and Bazant, Z. P. (1987). Non local damage theory. *Journal of Engineering Mechanics*, 113(10):1512–1533.

[Pijaudier-Cabot and Mazars, 2001] Pijaudier-Cabot, G. and Mazars, J. (2001). *Lemaitre Handbook of Materials Behavior Models*, chapter Damage Models for Concrete, pages 501–512. Academic Press.

[Pudasaini and Hutter, 2007] Pudasaini, S. P. and Hutter, K. (2007). *Avalanche Dynamics*. Springer.

[Sovilla et al., 2016] Sovilla, B., Faug, T., Köhler, A., Baroudi, D., Fischer, J.-T., and Thibert, E. (2016). Gravitational wet avalanche pressure on pylon-like structures. *Cold Regions Science and Technology*, 126:66 – 75.

[Sovilla et al., 2008] Sovilla, B., Schaer, M., Kern, M., and Bartelt, P. (2008). Impact pressures and flow regimes in dense snow avalanches observed at the vallée de la sionne test site. *Journal of Geophysical Research: Earth Surface*, 113(F1).

[Tanné et al., 2018] Tanné, E., Li, T., Bourdin, B., Marigo, J.-J., and Maurini, C. (2018). Crack nucleation in variational phase-field models of brittle fracture. *Journal of the Mechanics and Physics of Solids*, 110:80 – 99.

[Thomas and Mielke, 2010] Thomas, M. and Mielke, A. (2010). Damage of nonlinearly elastic materials at small strain – Existence and Regularity results. *ZAMM. Z. Angew Math. Mech.*, 90(2):88–112.

## List of Figures

|   |   |    |
|---|---|----|
| 1 | Sound and damaged domains, respectively $\Omega_0$ and $\Omega_1$ of the solid $\Omega$ . . . . .   | 6  |
| 2 | Clamped beam and axes . . . . .   | 8  |
| 3 | J and its derivative $J'$ functions of $P_{0,i}$ , from equations (21) and (22) . . . . .   | 13 |
| 4 | Evolution of the critical load, function of the previous state $\alpha_{i-1}$ (left) and evolution of the damage state, function of the load $P_{0,i}$ (right). . . . . | 13 |
| 5 | Relative error for the critical pressure $P_{\min}$ with respect to the mesh size. . . . .  | 17 |
| 6 | Dissipated energy by damage . . . . .   | 18 |

---

|    |   |    |
|----|---|----|
| 7  | Damage part of the beam at $P=40000$ Pa for different sizes of the grid . . . . .   | 18 |
| 8  | Damage part of the beam at $P=40000$ Pa for varying $\Delta P$ . . . . .  | 19 |
| 9  | Load history, percentage of damaged beam and maximum bending . . . . .  | 20 |
| 10 | Tension-Compression model: configuration of the tension experiment (left), pressure load (center left), damage function in percentage (center right) and the displacement $U$ at the F point (right). . . . .   | 25 |
| 11 | Comparison between different sizes of mesh with constant $\Delta P = 10000$ Pa: scenario of charge (left), displacement ( $U$ ) at the top point (center) and damage evolution in percentage (right). . . . .   | 26 |
| 12 | Comparison between different load steps with constant size of grid: scenario of charge (left), $U$ at the top point (center) and damage evolution (right). . . . .  | 26 |
| 13 | $P$ , $\chi_t$ for the tension experiment with different values of $E_1$ parameters from $2.10^9$ Pa to $2.10^3$ Pa . . .   | 27 |
| 14 | $\chi_t$ evolution from the first damage state . . . . .  | 28 |
| 15 | Corresponding VMS evolution during the tensile test without initial default . . . . .   | 28 |
| 16 | $\chi_t$ evolution from the first damage state with an initial default . . . . .  | 29 |
| 17 | Corresponding VMS evolution during the tensile test with an initial default . . . . .   | 29 |
| 18 | Traction-compression Model: tension-compression cycle. Applied load $P$ , evolution of damage $\chi_t$ and $\chi_c$ , displacement at the top of the beam $U$ and the stress $\sigma$ with respect to the strain $\epsilon$ (values of $\sigma$ and $\epsilon$ are taken at the central point). . . . . | 30 |
| 19 | TC Model: tension-compression cycle. $\chi_t$ at load 29 (left), $\chi_c$ at load 31 (center) at the onset of the damage and corresponding VMS field (right, load 30). . . . .  | 31 |
| 20 | TC Model: tension-compression cycle. $\chi_t$ (left), $\chi_c$ (center) and VMS field (right) at load 32. . . . .   | 31 |
| 21 | TC Model: tension-compression cycle. $\chi_t$ (left), $\chi_c$ (center) and VMS field (right) at load 60. . . . .   | 32 |
| 22 | TC Model: tension-compression cycle. $\chi_t$ (left), $\chi_c$ (center) and VMS field (right) at load 99. . . . .   | 32 |
| 23 | TC Model: tension-compression cycle. $P$ , $\chi$ , $U$ et $\sigma/\epsilon$ (values of $\sigma$ and $\epsilon$ are taken at the central point). . . . .  | 33 |
| 24 | TC Model: tension-compression cycle. $P$ , $\chi$ , $U$ and $\sigma/\epsilon$ , for $E_1 = 2.10^9$ Pa (values of $\sigma$ and $\epsilon$ are taken at the central point) . . . . .  | 34 |
| 25 | TC Model: tension-compression cycle. Evolution of $\sigma_{11}$ , $\sigma_{22}$ (left), $\epsilon_{11}$ and $\epsilon_{22}$ during the loads (center), $\sigma/\epsilon$ for $E_1 = 2.10^8$ Pa (right) (values of $\sigma$ and $\epsilon$ are taken at the central point). . . . .                      | 34 |
| 26 | Comparison of different mesh size . . . . .   | 35 |
| 27 | Damage in tension (left) and in compression (right) for different values of the threshold in compression. . . . .   | 35 |
| 28 | Configuration of the three-point flexural experiment . . . . .  | 36 |
| 29 | Load scenario and Damage fields . . . . .   | 36 |
| 30 | $\chi$ in tension (left) and VMS (right) fields at the onset of the damage . . . . .  | 37 |
| 31 | $\chi$ in tension (left) and VMS (right) fields during the propagation of the damage . . . . .  | 37 |
| 32 | $\chi$ in tension fields with the grid x10 . . . . .  | 38 |
| 33 | Load schemes and damage zone of the beam . . . . .  | 39 |

---

|    |   |    |
|----|---|----|
| 34 | VMS stress at loads 9, 11 and 14 . . . . .                                  | 40 |
| 35 | Damage area in tension: $\chi_t$ field at loads 9, 11 and 14 . . . . .      | 41 |
| 36 | VMS stress at loads 18, 20 and 21 . . . . .                                 | 42 |
| 37 | Damage area in compression: $\chi_t$ field at loads 18, 20 and 21 . . . . . | 43 |

## List of Tables

|   |   |    |
|---|---|----|
| 1 | Characteristic parameters of a 1-D beam for numerical illustrations . . . . . | 12 |
| 2 | Characteristic parameters of a 2-D beam for numerical illustrations . . . . . | 24 |